Progress in Nuclear Magnetic Resonance Spectroscopy 101 (2017) 71–95

Contents lists available at ScienceDirect

Progress in Nuclear Magnetic Resonance Spectroscopy

journal homepage: www.elsevier.com/locate/pnmrs

Recent advances in parallel imaging for MRI

Jesse Hamilton [a,*], Dominique Franson [a], Nicole Seiberlich [a,b]

[a] Biomedical Engineering, Case Western Reserve University, Cleveland, OH, USA
[b] Radiology, University Hospitals Cleveland Medical Center, Cleveland, OH, USA

Edited by David Gadian and David Neuhaus

ARTICLE INFO

Article history:
Received 30 January 2017
Accepted 17 April 2017
Available online 2 May 2017

Keywords:
Parallel imaging
Non-Cartesian
Simultaneous multi-slice
Spectroscopic imaging
Phase-constrained

ABSTRACT

Magnetic Resonance Imaging (MRI) is an essential technology in modern medicine. However, one of its main drawbacks is the long scan time needed to localize the MR signal in space to generate an image. This review article summarizes some basic principles and recent developments in parallel imaging, a class of image reconstruction techniques for shortening scan time. First, the fundamentals of MRI data acquisition are covered, including the concepts of k-space, undersampling, and aliasing. It is demonstrated that scan time can be reduced by sampling a smaller number of phase encoding lines in k-space; however, without further processing, the resulting images will be degraded by aliasing artifacts. Nearly all modern clinical scanners acquire data from multiple independent receiver coil arrays. Parallel imaging methods exploit properties of these coil arrays to separate aliased pixels in the image domain or to estimate missing k-space data using knowledge of nearby acquired k-space points. Three parallel imaging methods—SENSE, GRAPPA, and SPIRiT—are described in detail, since they are employed clinically and form the foundation for more advanced methods. These techniques can be extended to non-Cartesian sampling patterns, where the collected k-space points do not fall on a rectangular grid. Non-Cartesian acquisitions have several beneficial properties, the most important being the appearance of incoherent aliasing artifacts. Recent advances in simultaneous multi-slice imaging are presented next, which use parallel imaging to disentangle images of several slices that have been acquired at once. Parallel imaging can also be employed to accelerate 3D MRI, in which a contiguous volume is scanned rather than sequential slices. Another class of phase-constrained parallel imaging methods takes advantage of both image magnitude and phase to achieve better reconstruction performance. Finally, some applications are presented of parallel imaging being used to accelerate MR Spectroscopic Imaging.

Contents

* Corresponding author.
E-mail addresses: jxh490@case.edu (J. Hamilton), dnf7@case.edu (D. Franson), nicole.seiberlich@case.edu (N. Seiberlich).

http://dx.doi.org/10.1016/j.pnmrs.2017.04.002
0079-6565/

1. Introduction

Magnetic Resonance Imaging (MRI) is an essential technology for modern medicine. MRI can be used to generate high-resolution anatomical and functional images, and it is relatively safe due to the lack of ionizing radiation. Furthermore, MRI is sensitive to many physical properties, including the relaxation times T_1 and T_2, diffusion, and flow. Image contrast can be weighted by these properties by adjusting the scan settings to highlight different anatomical or physiological features.

However, the flexibility of MRI comes at the expense of long scan times compared to other imaging modalities. Spatial localization of the MRI signal is one of the main reasons for this long scan time. The basic steps of every pulse sequence – radiofrequency excitation, gradient encoding, and data acquisition – must be repeated many times to generate an image. The time needed to acquire an image can range from hundreds of milliseconds or less for certain scans, such as fast gradient echo or echo planar imaging (EPI), up to several minutes for spin echo or diffusion-weighted sequences.

This review summarizes key recent developments in parallel imaging, a class of image reconstruction methods that can be used to reduce scan time. Parallel imaging reconstructions are employed in nearly every clinical MRI scan to enable fast data collection, a necessity for many applications. These methods can be used to shorten the total scan time to improve patient compliance, which is vital for pediatric patients [1] and patients with neurodegenerative [2] diseases. Many abdominal and cardiac scans are acquired while patients hold their breath, and faster imaging makes breath holds easier to perform, particularly for sick patients. Savings in scan time can be invested in enhancing the spatial resolution or increasing the volumetric coverage. Some sequences, such as EPI and turbo spin echo (TSE), are prone to artifacts because many k-space lines are collected after each excitation pulse. Parallel imaging methods reduce the echo train length, which decreases blurring from T_2^* or T_2 effects and geometric distortion [3,4]. Rapid imaging is critical for dynamic imaging, such as real-time visualization of organs or interventional procedures [5], dynamic contrast enhanced MRI [6], and functional MRI (fMRI) for monitoring brain activity [7].

The goal of this manuscript is to provide the reader with a fundamental understanding of parallel imaging, and to explore some recently developed extensions to these techniques and their applications. First, a review of MRI data acquisition including the basics ideas of k-space, undersampling, and aliasing artifacts is presented. Next, SENSE, GRAPPA, and SPIRiT are introduced; these techniques form the foundation for other advanced parallel imaging methods. Finally, more recent developments including simultaneous multi-slice (SMS) imaging, CAIPIRINHA, non-Cartesian parallel imaging, and parallel imaging in conjunction with spectroscopic imaging are presented.

2. Data acquisition in MRI

MRI is a form of Nuclear Magnetic Resonance (NMR), its distinct feature being that MRI localizes signals in space to generate an image. The positions of spins are determined by linking their precession frequencies to their spatial locations, which is accomplished by employing magnetic field gradients. After exciting spins with a radiofrequency (RF) pulse, a magnetic field gradient is applied along one direction while signal is collected, a process called "frequency encoding". The gradient introduces a linear variation in spin precession frequency so there is a one-to-one correspondence between frequency and position, neglecting chemical shift effects. The receiver coils used in MRI acquire signals over the entire imaging volume, so the net received signal contains a mixture of many frequencies. The Fourier Transform is used to decompose the signal into its component frequencies in order to create a 1D projection image. However, frequency encoding can only localize signals along one spatial dimension; other dimensions are localized using a mechanism known as phase encoding. An additional gradient is briefly applied along a direction perpendicular to the frequency encoding direction after RF excitation. The gradient imparts a position-dependent phase across the object, which depends on the gradient strength and duration. This phase does not change while the frequency encoding gradient is applied in the perpendicular direction, resulting in data that are encoded in two spatial dimensions. A 2D image is formed by repeating the processes of RF excitation, phase encoding, and frequency encoding many times, stepping through different values for the phase encoding gradient. Note that a third spatial dimension may also be localized using a second phase encoding gradient to image a 3D volume.

The raw MRI data resulting from these applied magnetic field gradients form a matrix of spatial frequencies called k-space, and an image can be generated by applying the 2D discrete Fourier

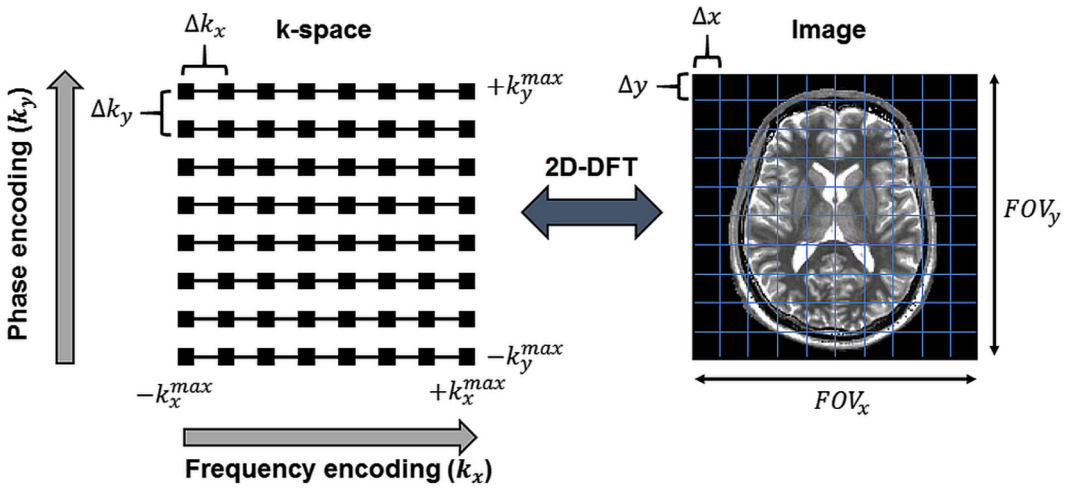

Fig. 1. MRI data are acquired in k-space, and an image is generated by applying a 2D discrete Fourier Transform to these data. The field-of-view (FOV) along x and y is inversely related to the spacing between adjacent k-space points, Δk_x and Δk_y. Likewise, the spatial resolution Δx and Δy is inversely related to the farthest excursion in k-space that is sampled, k_x^{max} and k_y^{max}.

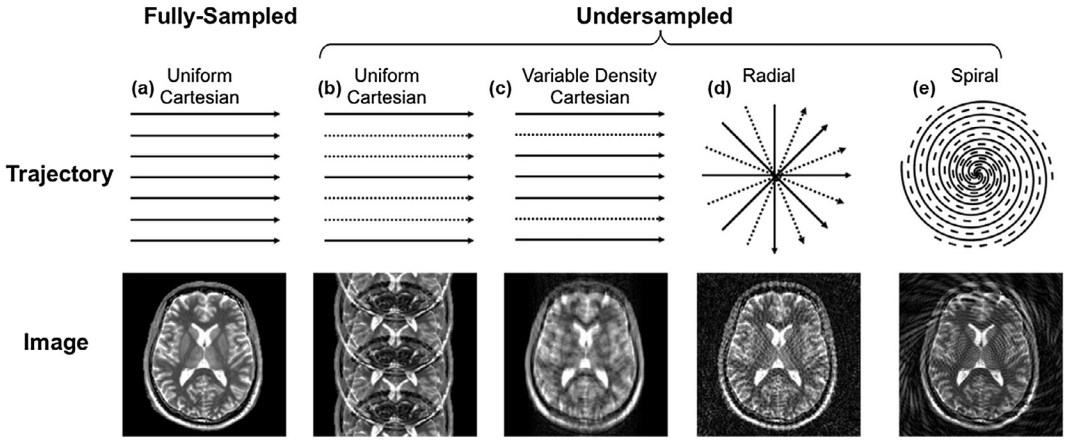

Fig. 2. Examples of different k-space trajectories and their associated aliasing artifacts. Acquired k-space data are indicated by solid lines, while missing data are depicted with dashed lines. (a) Fully-sampled Cartesian data produces a full FOV image. (b) Uniformly undersampled Cartesian k-space with an acceleration factor of R = 3 leads to coherent aliasing artifacts. (c) With variable density sampling, a higher concentration of lines is acquired near the k-space center, and the imaging artifacts are more diffuse. (d) Radial data can be undersampled by skipping radial spokes at regular intervals, which leads to diffuse streaking artifacts. (e) Spiral k-space can be undersampled by skipping spiral arms, which produces incoherent swirling artifacts.

Transform to these data [8]. The desired spatial resolution and field-of-view (FOV) dictate how much k-space data should be acquired (Fig. 1). The spacing between adjacent k-space lines is inversely related to the FOV:

$$FOV = \frac{1}{\Delta k} \tag{1}$$

To increase the FOV along one direction, the spacing between sampled k-space points must decrease. The Nyquist Sampling Theorem states that the FOV should be larger than the object size to avoid aliasing. If this condition is not satisfied, high-frequency signals will falsely appear as lower frequency signals. Because frequency information is used to determine spatial position, any part of the object outside the encoded FOV will be superimposed on signals from within the FOV, producing aliasing artifacts.

The spatial resolution is inversely proportional to the distance between the origin and the maximum extent of k-space (k_{max})

$$\Delta x = \frac{1}{2k_{max}} \tag{2}$$

To improve the spatial resolution, k-space points farther from the origin must be sampled.

Usually, k-space points are sampled on a Cartesian grid by collecting one phase encoding (k_y) line each repetition time (TR). The total acquisition time (TA) is determined by the TR, the number of acquired phase encoding lines (N_y), and the number of signal averages (N_A)

$$TA = N_y \cdot TR \cdot N_A \tag{3}$$

Note that in imaging, the number of averages is usually set to one for the sake of speed, and thus this is not a parameter that can typically be further reduced. Thus, this equation suggests two ways to reduce the total scan time. First, the TR may be shortened. However, the TR affects image contrast and is restricted by the type of pulse sequence used for imaging. Fast gradient echo scans use TRs on the order of milliseconds, while spin echo or diffusion-weighted sequences require much longer TRs. Rapid gradient switching is needed to attain short TRs, which risks inducing peripheral nerve stimulation [9–11]. Short TR sequences may

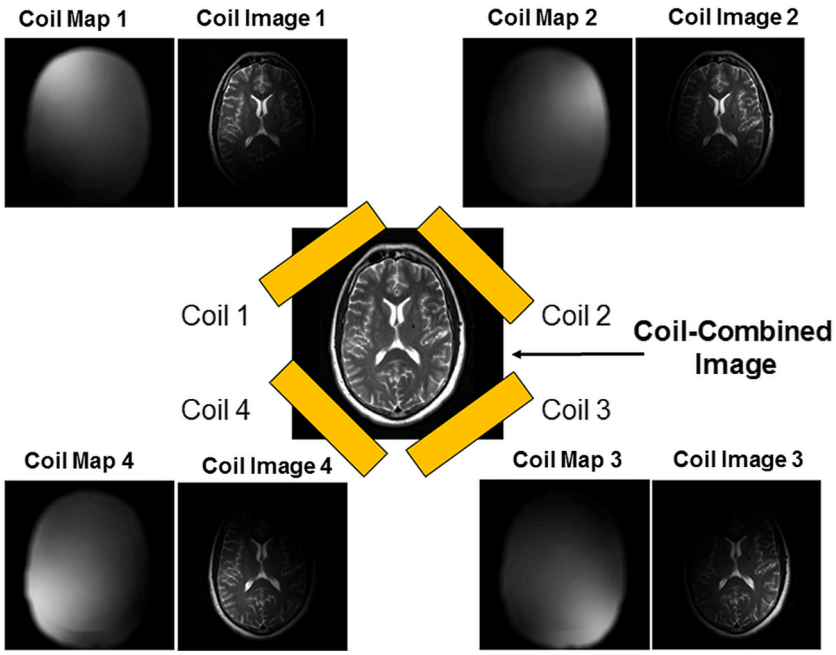

Fig. 3. The signal received by each coil in a receiver array consists of the magnetization weighted by the coil's sensitivity profile. The single-channel images can be combined to yield a single coil-combined image (right).

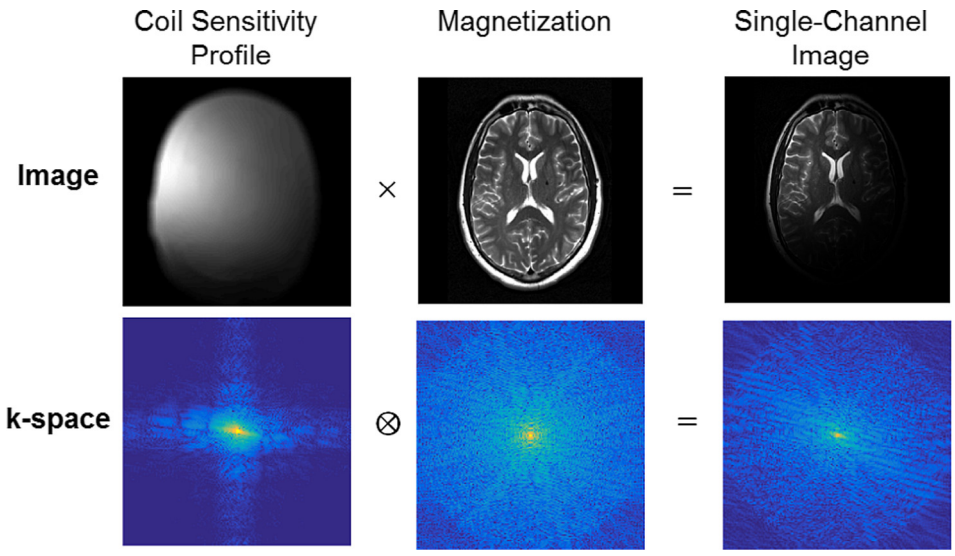

Fig. 4. The effects of an inhomogeneous receiver profile can be modeled in the image domain as a multiplication of the magnetization and the coil sensitivity profile. In k-space, this corresponds to a convolution between the coil sensitivity spectrum and the Fourier Transform of the image, which smears information throughout k-space.

deposit large amounts of RF energy into the patient [12]. There are also hardware limitations that restrict the minimum TR, like maximum gradient amplitude and slew rate.

Rather than shortening the TR, another option would be to reduce the number of lines collected in the phase encoding direction (i.e. acquire fewer k_y lines). One simple form of undersampling is to decrease k_{max} by collecting a smaller number of k-space lines all near the center of k-space. However, this will degrade the spatial resolution, which may lead to non-diagnostic images. Another option is to skip phase encoding lines at regular intervals (Fig. 2). The amount of undersampling is described by the acceleration factor R, defined as the ratio between the number of k-space points in the fully-sampled data compared to the undersampled data. Undersampling increases the spacing between adjacent k-space lines, which decreases the effective FOV. This results in coherent aliasing artifacts where replicates of the object appear at equally spaced intervals in the reduced FOV image, with the number of replicates equal to the acceleration factor (Fig. 2b).

The goal of parallel imaging is to remove the aliasing artifacts that result from undersampling phase encoding lines in k-space. There are a number of different parallel imaging techniques, although they all share the same basic principles, which are described below.

3. Phased array coils and basic principles of parallel imaging

Parallel imaging requires special hardware known as phased array coils that are now supplied with nearly every modern clinical

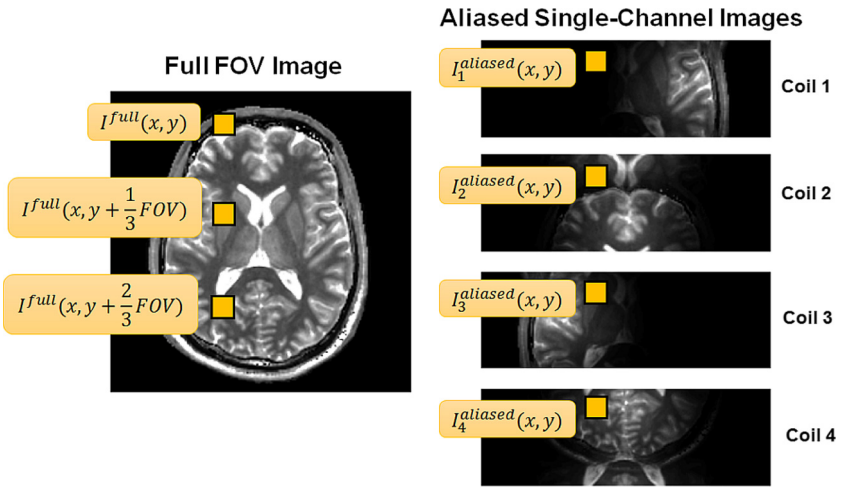

Fig. 5. Schematic of a SENSE reconstruction for a uniform Cartesian acceleration of R = 3 with four coils. Signal from three equally spaced pixels in the object (left) are aliased onto the same pixel in the reduced FOV images.

scanner. Phased arrays contain multiple independent receiver channels [13]. Each coil element is most sensitive to the magnetization closest to it and less sensitive to magnetization further away. The spatial sensitivity can be visualized as the coil's sensitivity profile (Fig. 3). Note that in these maps, the coil sensitivity falls off rapidly with increasing distance from the coil. Individually, each coil has high local signal-to-noise ratio (SNR) but inhomogeneous coverage. To expand the FOV while maintaining high SNR, several coils are organized in an array. The images from each channel are usually combined into a single image with relatively homogeneous intensity by taking a root sum-of-squares combination or using more advanced methods that preserve SNR [14]. Dedicated surface coil arrays are provided for different parts of the body. Coil arrays can have up to 32 [15,16], 64 [17], or 96 [18] channels for brain imaging or 128 channels for cardiac imaging [19], although most high-count arrays are still in research development.

Intuitively, every coil can be used to generate a unique view of the object, which provides additional spatial information that can partially replace gradient encoding to reduce scan time. Each coil detects signals from the object weighted by the coil's sensitivity profile (Fig. 4). This weighting can be modeled as a multiplication of the coil sensitivity profile and the magnetization. The use of a coil with an inhomogeneous sensitivity also affects k-space. Multiplication in the image domain is equivalent to convolution in the frequency domain. Therefore, in k-space the Fourier Transform of the image is convolved with the spectrum of each coil's sensitivity profile.

Theoretically, the maximum acceleration factor is limited by the number of coils, as will be explained in the SENSE section. For parallel imaging to be successful, each coil must have a unique sensitivity variation along the direction that is accelerated. For example, an array with four coils arranged in a line may be able to attain a maximum R = 4 along one direction, but no acceleration would be possible in the perpendicular direction.

4. Representative parallel imaging techniques: SENSE, GRAPPA, and SPIRiT

Parallel imaging techniques fall into one of two classes, depending on whether aliased pixels are separated in the image domain (as in SENSE) or missing phase encoding lines are reconstructed in k-space (as in GRAPPA). These methods are described next, as they are the techniques most commonly used in clinical practice. SPIRiT and its extensions will also be covered to highlight the connection between image domain and k-space reconstructions.

4.1. SENSE

SENSitivity Encoding (SENSE) is a parallel imaging technique which unfolds superimposed pixels in the image domain [20]. Consider an example with Cartesian k-space sampling, a uniform acceleration factor of R = 3, and a receiver array with four coils (Fig. 5). Undersampling reduces the FOV threefold, such that three pixels from the fully-sampled image fold onto the same pixel in the aliased image. SENSE uses prior knowledge of the coil sensitivity profiles to separate folded pixels and recover the full FOV image.

The first step in the SENSE reconstruction is to form a sensitivity matrix S for a given pixel in the aliased image. This matrix has size $n_c \times n_p$, where n_C is the number of coils and n_p is the number of aliased pixels, which is equal to the acceleration factor. Let the signal at location (x,y) in the aliased dataset received by coil j be denoted $I_j^{aliased}(x,y)$. It can be expressed as the sum of three pixels in the full FOV image that have been weighted by their coil sensitivities and are separated by distance $FOV/3$.

$$\begin{bmatrix} I_1^{aliased}(x,y) \\ I_2^{aliased}(x,y) \\ I_3^{aliased}(x,y) \\ I_4^{aliased}(x,y) \end{bmatrix} = \begin{bmatrix} S_1(x,y) & S_1(x,y+\frac{1}{3}FOV) & S_1(x,y+\frac{2}{3}FOV) \\ S_2(x,y) & S_2(x,y+\frac{1}{3}FOV) & S_2(x,y+\frac{2}{3}FOV) \\ S_3(x,y) & S_3(x,y+\frac{1}{3}FOV) & S_3(x,y+\frac{2}{3}FOV) \\ S_4(x,y) & S_4(x,y+\frac{1}{3}FOV) & S_4(x,y+\frac{2}{3}FOV) \end{bmatrix} \begin{bmatrix} I_{full}(x,y) \\ I_{full}(x,y+\frac{1}{3}FOV) \\ I_{full}(x,y+\frac{2}{3}FOV) \end{bmatrix} \quad (4)$$

This equation can be written more compactly as

$$\boldsymbol{a} = S\boldsymbol{v} \quad (5)$$

where $\boldsymbol{v}$ has size $n_p \times 1$ and contains the unfolded image pixels, and $\boldsymbol{a}$ has size $n_C \times 1$ and contains the signals at one location from all coils in the aliased image. When the sensitivity matrix is square and invertible, the equations can be solved by multiplying each side by S^{-1}. Otherwise, the pseudoinverse of the sensitivity matrix (called the unfolding matrix) is used

$$\boldsymbol{v} = (S^H S)^{-1} S^H \boldsymbol{a} \quad (6)$$

If the acceleration factor exceeds the number of coils, then the SENSE equations will not be invertible. In practice, the largest achievable acceleration factor is usually smaller than the theoretical limit because coil sensitivities overlap and are not orthogonal.

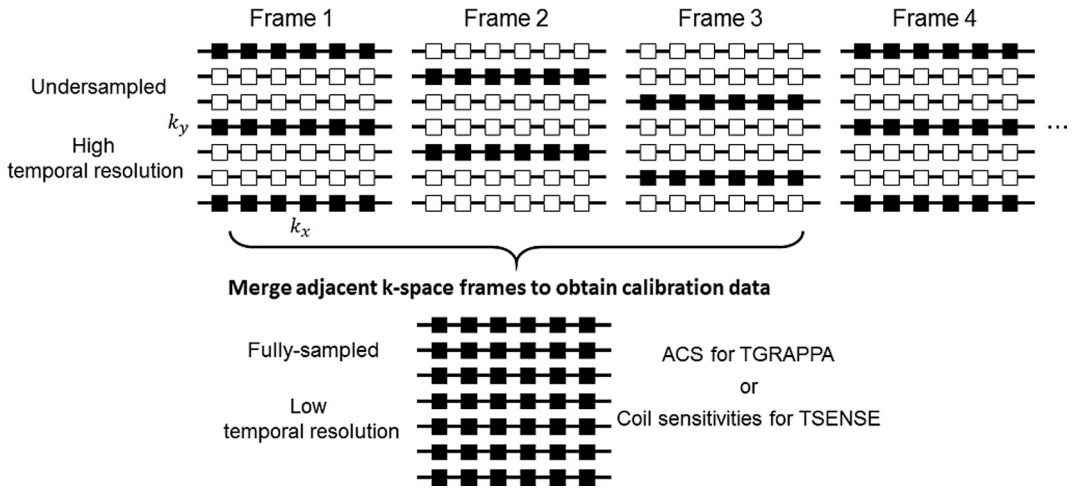

Fig. 6. In TSENSE and TGRAPPA, dynamic data are acquired using a time-interleaved sampling scheme that collects different phase encoding lines for each image frame. Coil sensitivity information for TSENSE or calibration data for TGRAPPA are obtained by merging adjacent k-space frames using a sliding window to produce a fully-sampled dataset, albeit with lower temporal resolution.

As mentioned earlier, the coil sensitivities must have variations along the accelerated direction for them to provide the spatial encoding required by the parallel imaging reconstruction.

The coil sensitivities needed for SENSE are typically measured during a prescan. Because sensitivity profiles usually have gradual intensity and phase changes, they can be measured quickly at a low spatial resolution. One approach is to acquire uncombined channel images at the full FOV and divide them by a root sum-of-squares image; a second option is to divide them by an image obtained with a body coil, which should have homogeneous sensitivity. The division removes anatomical features and only leaves the coil sensitivity information. Next, the sensitivity profiles may be lowpass filtered or fitted to a polynomial model to reduce noise, and they can be extrapolated beyond the object and into areas with low signal.

Some variants of SENSE use coil maps extracted from the accelerated data and are termed auto-calibrating. In time-adaptive sensitivity encoding or TSENSE, k-space is undersampled using an interleaved trajectory (Fig. 6) [21]. Several undersampled k-space frames are merged to produce a fully-sampled k-space, which has a longer temporal footprint but is sufficient to estimate the coil sensitivities. TSENSE is effective even if the coils move slightly during the acquisition, for example due to breathing, since the sensitivities are updated dynamically. In other auto-calibrating techniques like mSENSE, coil sensitivities are estimated by acquiring a few additional lines near the center of k-space to generate low-resolution reference images [22].

One common feature of parallel imaging is that noise in the reconstructed image is amplified, and the degree of amplification varies over the image. The geometry factor, or g-factor, describes the spatial pattern of noise enhancement. The g-factor depends on many variables, including the number of coils, array configuration, coil loading, and scan plane orientation. The signal-to-noise ratio in the reconstructed SENSE image ($SNR_{accelerated}$) is related to that of the fully-sampled image (SNR_{full}) according to

$$SNR_{accelerated}(x,y) = \frac{SNR_{full}(x,y)}{g(x,y)\sqrt{R}} \tag{7}$$

In addition to g-factor losses, SNR decreases with the square root of the acceleration factor. This effect is known as Fourier averaging in signal processing, where SNR scales with the square root of the number of measurements. This loss in SNR is not unique to SENSE and is an unavoidable feature of all parallel imaging methods.

There are several optional processing steps that can improve images reconstructed with SENSE. Noise properties of the receiver array can be incorporated into the reconstruction to improve the SNR and lower the g-factor. Tikhonov or total variation regularization can also be performed to improve the conditioning of the inverse problem [23–25]. Regularization reduces noise amplification but may lead to residual aliasing if applied too heavily.

SENSE is one of the two main parallel imaging methods used routinely in the clinic (the other is GRAPPA). The reconstruction is provided by most MRI scanner manufacturers, and many scans are customarily accelerated by a factor of two or three. Most vendor implementations are able to display the reconstructed images immediately after data collection. The following is a sampling of clinical applications where SENSE is used to reduce scan time or improve spatial resolution. SENSE has been applied to accelerate whole-brain dynamic contrast enhanced exams [26]. Retrospective cardiac CINE images have been generated using TSENSE with motion correction [27] and SENSE combined with compressed sensing [28]. Real-time cardiac imaging can be performed with temporal resolutions as high as 13 ms per frame [29], and SENSE can enable whole-heart visualization of coronary arteries [30]. One study found that scan time for musculoskeletal exams can be reduced by half without compromising diagnostic quality [31]. SENSE is also used in MR Angiography (MRA) exams to visualize intracranial vessels [32], abdominal vasculature [33–35], and peripheral vessels [36].

4.2. GRAPPA

Whereas SENSE unfolds aliased signals in the image domain, GeneRalized Partially Parallel Acquisitions (GRAPPA) synthesizes missing data points directly in k-space [37]. As described above and shown in Fig. 3, collecting data with multiple inhomogeneous receiver coils weights the magnetization by each coil's sensitivity profile. In k-space, the use of inhomogeneous receiver coils effectively "spreads" information from one k-space point to nearby k-space points (Fig. 4). GRAPPA exploits these k-space redundancies across coils to reconstruct missing k-space data using neighboring acquired points.

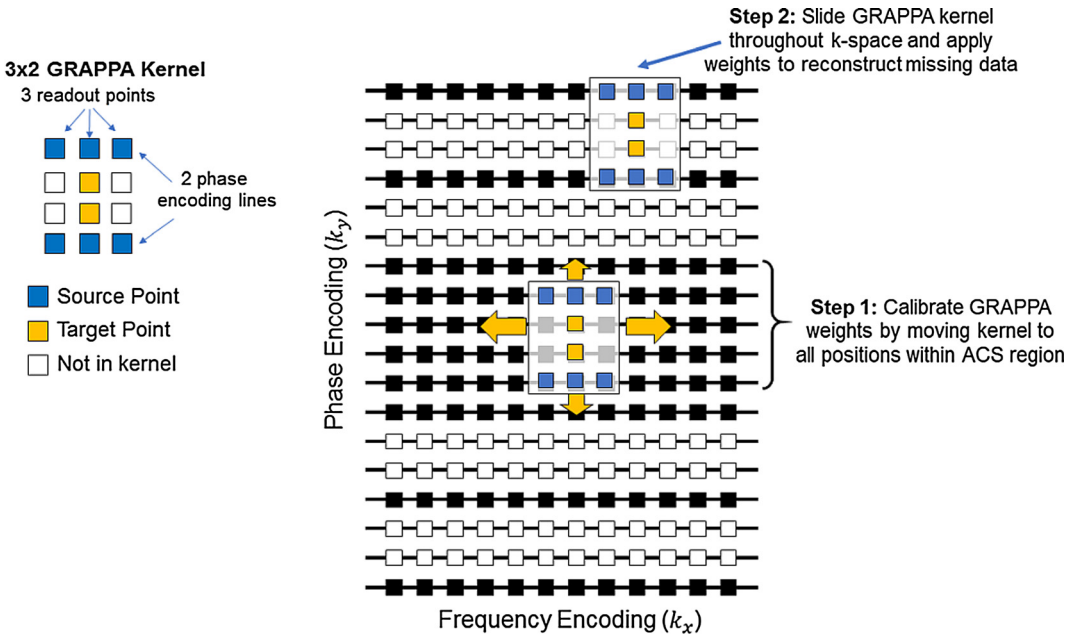

Fig. 7. Schematic of the GRAPPA reconstruction. (a) An example GRAPPA kernel for the reconstruction of Cartesian data undersampled by a factor R = 3. The kernel contains source points from three readout points and two phase encoding lines (a so-called 3 × 2 kernel). Although not shown in the diagram, the kernel uses source points from all coils to synthesize target points in one coil. (b) For GRAPPA calibration, several additional lines are collected at the center of k-space (the ACS region) to estimate the GRAPPA weights (Step 1). The weights are then used to synthesize the undersampled parts of k-space (Step 2).

In GRAPPA, a single missing k-space data point, called a target point, is synthesized as a linear combination of acquired neighboring k-space points, called source points. The spatial arrangement of source and target points is called the GRAPPA kernel. Each acquired source point is multiplied by a coefficient, or GRAPPA weight, and the results are added to estimate the target point. A single target point for one coil is reconstructed using source points from all other coils. This process can be represented mathematically as

$$s_{targ,i}(k_x, k_y + \Delta k_y) = \sum_{j=1}^{n_c} \sum_{\tau_x} \sum_{\tau_y} w(i, j, \tau_x, \tau_y) \cdot s_{src,j}(k_x + \tau_x, k_y + \tau_y) \tag{8}$$

where i is the coil index for the target point, j is the coil index for the source point, τ_x and τ_y denote the position of the source points within the kernel, and w is the weight for a given source point. For Cartesian acquisitions, the weights are shift invariant to a first approximation, so the same GRAPPA weights can be applied throughout k-space. For every unacquired k-space point, the reconstruction may be written in matrix form as

$$S_{targ} = W \cdot S_{src} \tag{9}$$

In this equation, S_{src} is a vector of source points with size $n_c n_k \times 1$ (where n_k is the kernel size, or number of k-space source points included in the kernel), S_{targ} is a vector of target points with size $n_c \times 1$, and W is a matrix of the GRAPPA weight set with size $n_c \times n_c n_k$.

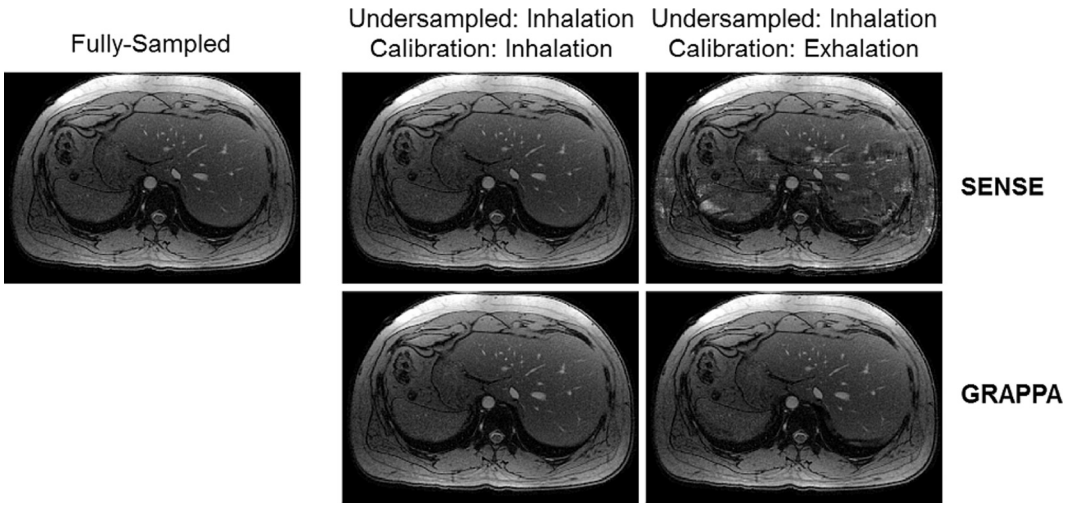

Fig. 8. Robustness of SENSE and GRAPPA to respiratory motion during calibration. Two fully-sampled Cartesian scans were acquired under breathhold conditions in end inspiration and end expiration. The data collected at end inspiration were retrospectively undersampled by a factor of R = 2. SENSE was performed using coil sensitivities derived from the inspiration (top left) and expiration (top right) scans. Likewise, a GRAPPA reconstruction was performed using the ACS data (the center 40 phase encoding lines) from the inspiration (bottom left) and expiration (bottom right) scans. The coil sensitivity mismatch between calibration and undersampled scans leads to noticeable residual aliasing in SENSE; less disruptive aliasing artifacts are seen in GRAPPA.

The reconstruction can be visualized as convolving or sliding the GRAPPA kernel throughout k-space; as the kernel moves from point to point, the weights are multiplied by the kernel source points to reconstruct the kernel's target points (Fig. 7). A typical kernel may consist of six source points from each coil, with three in the readout direction and two in the phase encoding direction, centered around a target point. Including more source points tends to improve the reconstruction quality [38] but may require additional calibration data, as discussed below.

While SENSE uses additional information in the form of coil sensitivity profiles to unfold aliased pixels, GRAPPA requires extra data to estimate the weight set. GRAPPA is considered to be "auto-calibrating" because several additional phase encoding lines, called the auto-calibration signal or ACS, are collected near the k-space origin for calculating the weights. The GRAPPA kernel is moved to every possible position within the ACS to accumulate many instances where the source points and target points are both known. Then the GRAPPA equation can be inverted to solve for the unknown weight set. To have an overdetermined system of equations, there must be more than $n_c n_k$ instances of the kernel geometry within the ACS. The GRAPPA weights will be more robust if more calibration data are collected since the system of equations will be more overdetermined and less susceptible to noise. If the ACS lines are collected as part of the accelerated scan, they may be included in the final reconstruction to improve image quality. Alternatively, the ACS data can be collected as a separate low-resolution scan, which will improve the temporal resolution of the undersampled data. GRAPPA has the interesting property that the weight sets are robust even if the calibration and undersampled scans have different sequence parameters. This is important for applications such as diffusion imaging or fMRI where the sequence requires long repetition times, but a fast sequence, such as Fast Low Angle Shot (FLASH), can be used for calibration [39].

The GRAPPA weights can also be calibrated dynamically during the scan using methods such as TGRAPPA [40]. Like TSENSE, k-space data are acquired with a time-interleaved sampling pattern (Fig. 6). Data from adjacent time frames are merged using a sliding window to form a low temporal resolution, fully-sampled k-space for calibrating the GRAPPA weights. The GRAPPA weights are then applied to the undersampled k-space frames to reconstruct images at the nominal temporal resolution. TGRAPPA allows for dynamic updates of the GRAPPA weights and is well-suited for free-breathing or real-time applications.

The SNR of images reconstructed using GRAPPA is also reduced according to Eq. (7). As in SENSE reconstructions, it is possible to generate g-factor maps for GRAPPA that quantify the amount of noise enhancement across the image. Whereas SENSE g-factor maps are derived from the sensitivity matrix, GRAPPA g-factor maps can be computed analytically from the GRAPPA kernel [41]. The g-factor maps can aid in choosing an optimal kernel size for a given coil configuration and loading.

Because GRAPPA does not require an explicit estimate of the coil sensitivities, it tends to be more robust than SENSE to inconsistencies between the calibration and undersampled data. Fig. 8 shows an example of an abdominal scan acquired at end inspiration with an acceleration factor of R = 2. Separate calibration data were collected at end expiration after the coil array had moved, which were used to estimate coil sensitivities for SENSE and the weight set for GRAPPA. The residual aliasing is much more pronounced in the images reconstructed with SENSE compared to GRAPPA, especially near the center of the image. It can also be difficult to measure coil sensitivities in areas with low signal, such as the lungs or sinuses. In addition, it is possible to use GRAPPA to reconstruct images even when the FOV is smaller than the size of the object [42]. SENSE reconstructions do not perform well in this case because the coil sensitivities themselves contain wraparound artifacts from parts of the object that lie outside the FOV. However, both techniques rely on the same basic information, namely coil sensitivity variations, to enable the reconstruction of unaliased images from undersampled data.

GRAPPA is robust and widely used clinically (like SENSE) to reduce acquisition time or improve spatial resolution. Like SENSE, most vendor implementations of GRAPPA are able to display reconstructed images almost immediately after acquisition. Some applications include cardiac CINE imaging with GRAPPA [43,44] or TGRAPPA [45] and dynamic imaging of swallowing and pharyngeal movement [46]. Interventional imaging requires high temporal resolutions and rapid scan plane reorientations that can be achieved with parallel imaging reconstructions like GRAPPA [47,48]. Spine protocols are notoriously long but can be shortened two- or threefold with GRAPPA [49–51]. GRAPPA has also been used to accelerate MRA exams [52,53]. In hyperpolarized MRI, GRAPPA is exploited to collect data quickly while polarization levels are still high [54,55]. Sequences such as EPI and TSE, which are commonly used for fMRI and diffusion imaging, are prone to blurring, distortion, and signal dropout due to long echo train lengths, which can be mitigated using GRAPPA [56–58]. Another interesting application of parallel imaging techniques such as GRAPPA is reducing acoustic noise for better patient comfort [59].

4.3. Self-consistent parallel imaging

4.3.1. SPIRiT

Iterative self-consistent parallel imaging (SPIRiT) [60] combines features of SENSE and GRAPPA. Like GRAPPA, SPIRiT uses k-space kernels to recover missing information by exploiting correlations between neighboring k-space points. However, the reconstruction is framed as an inverse problem like SENSE. Regardless of the original sampling trajectory, the output of SPIRiT is a Cartesian k-space. The SPIRiT reconstruction is typically initialized with the zero-filled and undersampled k-space, and it is solved iteratively as an optimization problem. On each iteration, the algorithm moves toward a solution that minimizes and balances the errors between two terms: calibration consistency and data consistency

The first error term is calculated using a k-space convolution kernel or SPIRiT kernel and is called the "calibration consistency" term. Recall that in GRAPPA, each target point is expressed as a weighted sum of nearby acquired points. SPIRiT conveys this relationship more generally, where every point on the final Cartesian grid is expressed as a weighted sum of all neighboring grid points, including data points that were synthesized and not originally acquired. This process is visualized as convolving or sliding the SPIRiT kernel throughout k-space. An example of a 5×5 kernel is shown in Fig. 9, which includes both collected and missing k-space points. If the correct solution is found, convolving a given k-space point with the SPIRiT kernel should produce the same k-space data, and the first error term will be zero. Like GRAPPA, SPIRiT requires additional calibration data to estimate the SPIRiT kernel coefficients. For Cartesian scans, the center of k-space is fully-sampled so that enough repetitions of the SPIRiT kernel can be accumulated by moving the kernel throughout this region.

The second term in the optimization enforces consistency with the undersampled data and is called the "data consistency" term. In other words, the reconstruction is allowed to recover missing k-space points but it should not change the acquired data points. At the originally sampled k-space positions, the difference between the reconstructed data and acquired data should be zero.

The SPIRiT reconstruction proceeds either for a fixed number of iterations or until the change between iterations falls below a certain threshold. Additional constraints can be incorporated into the cost function to improve the final image quality. These may include

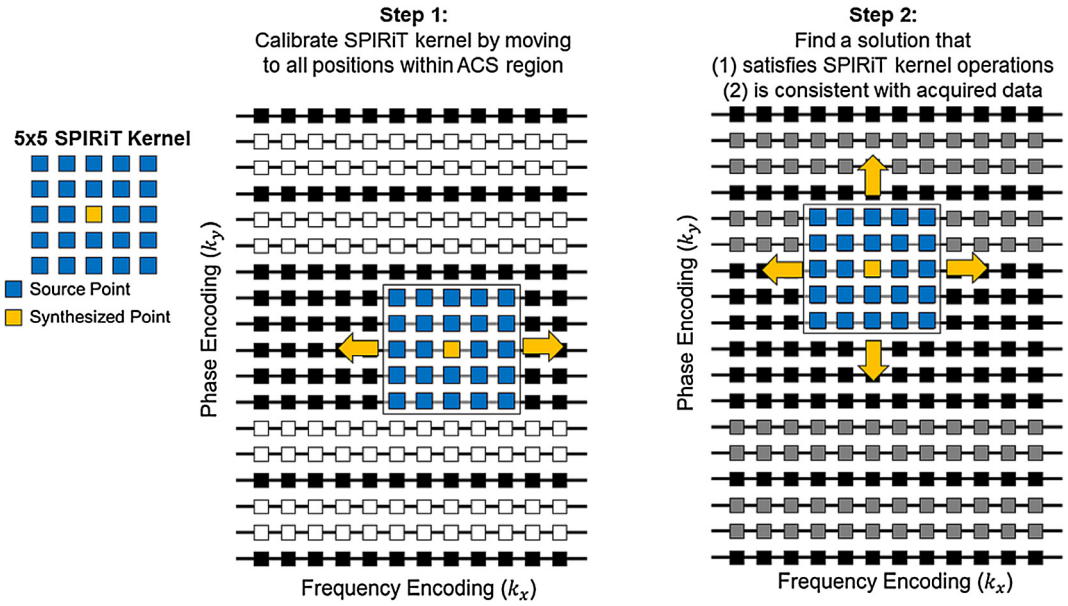

Fig. 9. Schematic of the SPIRiT reconstruction. SPIRiT reconstructs data onto a Cartesian k-space grid. A SPIRiT kernel (left) is defined where each target point (shown in yellow) is expressed as a linear combination of all surrounding grid points (shown in blue), including both points that were originally acquired and points that were synthesized during the reconstruction. The SPIRiT kernel is calibrated using a fully-sampled region near the center of k-space (Step 1). Then a solution is found that satisfies the SPIRiT kernel relationships and is consistent with the acquired data (Step 2). (For interpretation of the references to color in this figure legend, the reader is referred to the web version of this article.)

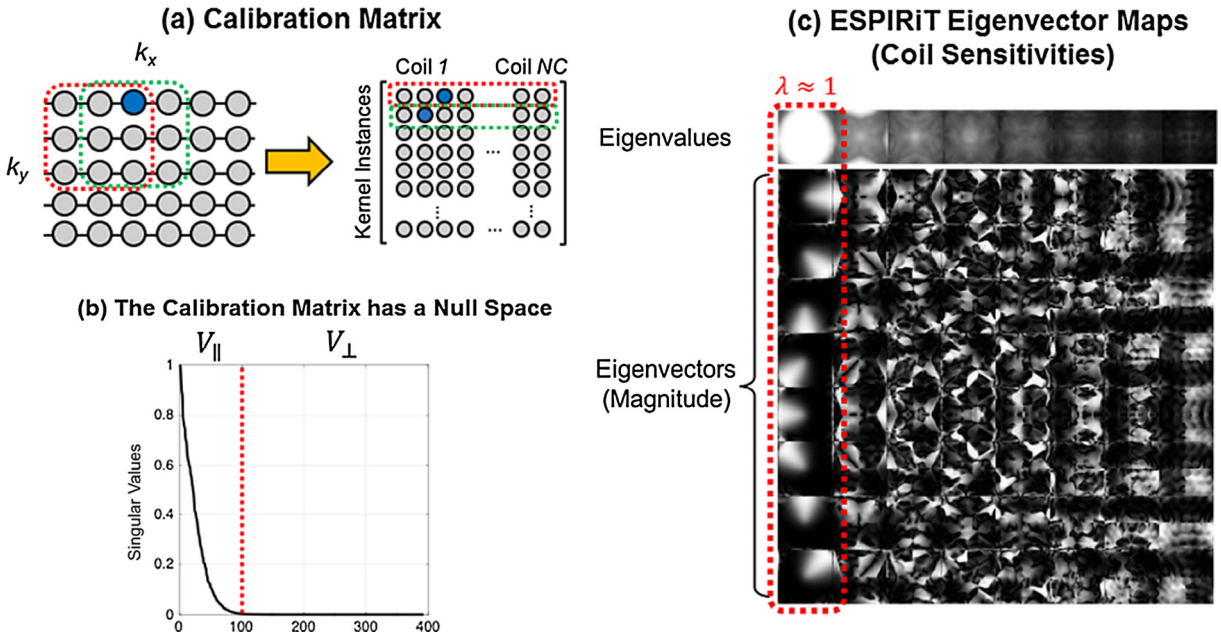

Fig. 10. Important features of the ESPIRiT reconstruction. (a) ESPIRiT requires calibration data from the center of k-space. A calibration matrix is created by sliding a kernel through this region and reshaping each kernel instance into a row of the matrix. (b) Many of the singular values of the calibration matrix are close to zero, meaning that this matrix has a null space. (c) Eigenvector maps can be derived from the calibration data. The dominant eigenvectors (leftmost column) behave like coil sensitivity maps. The non-dominant eigenvectors (all other columns) can be thought of as "soft" sensitivity maps and can be used in a relaxed SENSE reconstruction.

terms for spatial regularization (e.g. wavelets as in l_1-SPIRiT [61]), off-resonance correction to reduce blurring, or noise correlations between coils to enhance SNR.

4.3.2. ESPIRiT

ESPIRiT is an extension of SPIRiT that provides insights into the connections between GRAPPA and SENSE [62]. Briefly, ESPIRiT uses k-space kernel operations to derive a set of eigenvector maps that behave like coil sensitivities, which can be incorporated in a generalized SENSE reconstruction.

ESPIRiT requires additional calibration data in the form of a fully-sampled region at the center of k-space. A k-space kernel is moved to each possible position within this region, and each instance of the kernel is reshaped to populate a row in a special matrix. Many of the singular values of this matrix are small or close to zero, meaning that it has a null space. The existence of a null space implies that neighboring k-space points in the multichannel data are correlated. Missing k-space data are reconstructed by recognizing that this relationship should be true not only over the calibration region but also over the entire k-space.

The calibration matrix from ESPIRiT can be used to derive coil sensitivity maps. An eigenvector decomposition of the calibration matrix produces a set of eigenvector maps as shown in Fig. 10. The eigenvectors behave like coil sensitivity profiles up to an arbitrary scaling factor. In most cases, there will be a set of eigenvectors with eigenvalues equal to one. These eigenvector maps have the appearance of conventional coil sensitivities and can be used in a SENSE reconstruction. Sometimes additional eigenvectors will have non-negligible eigenvalues, meaning that some data cannot be described by the SENSE model. This may happen if there are inconsistencies from motion or if the FOV is smaller than the object. In this case, multiple sets of sensitivity maps can be included in a relaxed or "soft" SENSE reconstruction. ESPIRiT with soft SENSE is like GRAPPA in that aliasing can be resolved even for small FOV imaging [42].

Although these techniques are not yet available on most MRI platforms, SPIRiT and its extensions have been used clinically for pediatric abdominal imaging and dynamic contrast exams, where fast imaging reduces the chances of young patients moving during the scan [63]. Unlike SENSE and GRAPPA, SPIRiT reconstructs images iteratively and can require long computation times. However, this time can be drastically reduced using parallelized computing and graphics processing units (GPUs). SPIRiT combined with compressed sensing and at-the-scanner reconstruction using coil compression has been explored for pediatric abdominal dynamic contrast-enhanced (DCE) [64]. Additionally, real-time free-breathing cardiac CINE imaging can be performed in under 20 s with SPIRiT [65].

5. Non-Cartesian parallel imaging

SENSE, GRAPPA, and SPIRiT were described for Cartesian sampling to introduce the basic principles of parallel imaging. However, these methods can be extended to other k-space sampling patterns, where the collected points do not fall on a rectangular grid. Some examples of these non-Cartesian trajectories are shown in Fig. 2. Non-Cartesian scans are undersampled by skipping certain readout lines (called projections), which splits the acceleration into both k_x and k_y directions. In contrast, Cartesian scans are typically accelerated along only one direction by skipping phase encoding lines. Non-Cartesian aliasing artifacts therefore appear noise-like and are less coherent than their Cartesian counterparts. Visually, it may be easier to see through the artifacts to discern the underlying image content. Non-Cartesian sampling may therefore put less burden on the parallel imaging reconstruction and thus permit higher acceleration factors.

Non-Cartesian trajectories have other attractive properties. They are usually less sensitive to motion due to the denser sampling near the center of k-space. Some trajectories, like spirals, use the gradient fields efficiently and can cover k-space in a shorter amount of time [66]. However, one disadvantage of non-Cartesian sampling is that the image reconstruction becomes more technically demanding. For instance, non-Cartesian k-space data must be transformed to images using the non-uniform Fourier Transform (NUFFT) [67], or convolution gridding [68] followed by the DFT. Similarly, parallel imaging reconstruction of accelerated non-Cartesian data is significantly more challenging than the reconstruction of Cartesian data.

5.1. Conjugate Gradient SENSE

Conjugate Gradient SENSE (CG SENSE) is a modification of SENSE for non-Cartesian trajectories [69]. Due to the irregular undersampling in k-space, each pixel in the aliased image can be contaminated with signals from potentially every other pixel, and the SENSE reconstruction becomes more challenging due to the large number of overlapping pixels that must be separated. The CG SENSE forward model can be written as

$$\boldsymbol{F} = E\boldsymbol{m} \tag{10}$$

where $\boldsymbol{F}$ is the vectorized k-space data of size $n_k n_c$ (with n_c coils and n_k total k-space points), and $\boldsymbol{m}$ is the vectorized image having size

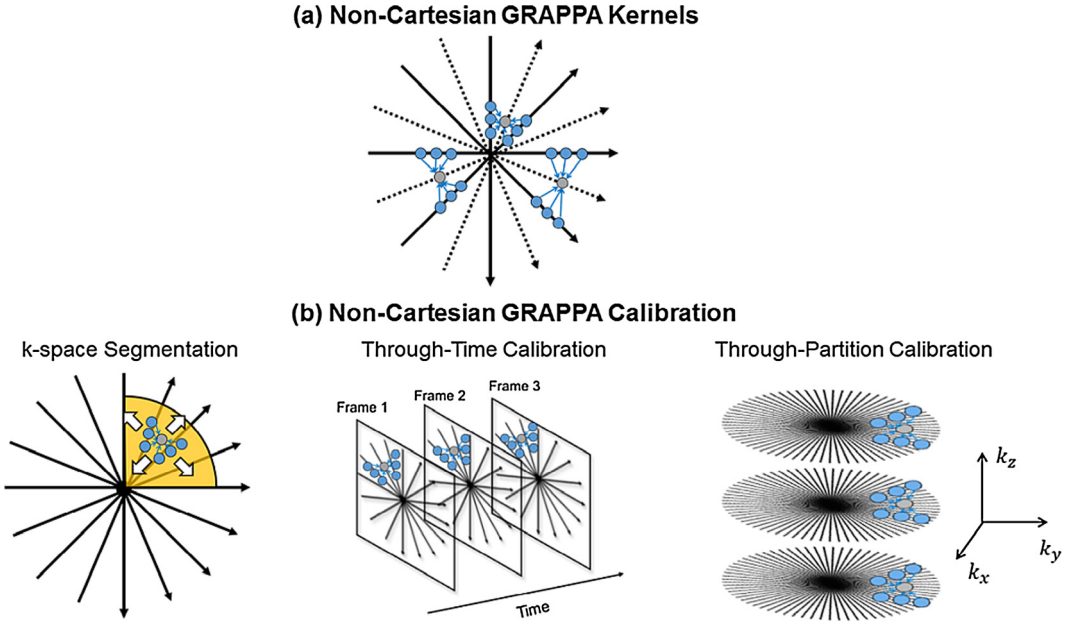

Fig. 11. (a) Non-Cartesian GRAPPA kernels change size and shape throughout k-space. Therefore, different GRAPPA weights must be estimated for each missing k-space point. (b) Three methods for the calibration of non-Cartesian GRAPPA weights are illustrated. All require that one or more fully-sampled 2D frames or 3D volumes of calibration data be collected. First, the calibration k-space may be divided into segments (typically smaller than illustrated here), and kernel instances are accumulated by sliding the kernel within each segment. Second, through-time calibration involves the collection of multiple fully-sampled calibration frames, and the kernel replicas are gathered through-time to generate enough data for calibration. Third, through-partition calibration can be used in 3D imaging where the kernel geometry is repeated across each partition, assuming data are acquired with a 3D cylindrical trajectory.

$n_p \times 1$, where n_p is the number of pixels. The encoding matrix E includes terms for coil sensitivities and spatial encoding. Theoretically, this equation could be inverted to solve for the unknown image pixels. However, the encoding matrix is enormous even for moderate image sizes, with size $n_c n_k \times n_p$. Consider a 256×256 image with 12 coils, where data are collected using a radial trajectory with 400 projections and 512 readout points. Then the encoding matrix would have dimensions $(12)(400)(512) \times (256)(256)$, or $2,457,600 \times 65,536$. Rather than explicitly writing E as a matrix, its effects on the data can be implemented using NUFFT operations and pixel wise multiplication by coil sensitivities. The reconstruction can be solved efficiently using conjugate gradient descent. Starting from some initial guess, typically a zero image or the undersampled image after gridding, the solution will progressively improve at each iteration until it converges.

CG SENSE has the advantage of being applicable to arbitrary k-space sampling patterns. However, like its Cartesian counterpart, CG SENSE requires accurate coil sensitivity maps. Any mismatch between the coil sensitivities and the undersampled data (e.g. due to motion) will lead to residual aliasing. Additional regularization terms can be included to improve the conditioning of the encoding matrix.

5.2. Non-Cartesian GRAPPA

In undersampled non-Cartesian datasets, there are different geometric relationships throughout k-space between collected (source) and missing (target) points (Fig. 11a). Thus, each missing point requires a different GRAPPA kernel and weight set. The need for a weight set for each missing point presents a challenge in collecting ACS data that contain enough instances of each kernel to solve for the unknown weight set. One approach is to collect fully-sampled data separately from the acquisition of the accelerated data (Fig. 11b). The instances for a particular kernel can then be gathered by moving the kernel inside a small segment of the fully-sampled k-space around the target point; by collecting several repetitions before or after the undersampled acquisition and gathering instances through time [70,71]; or by collecting instances over many partitions of k-space, in the case of 3D datasets [72]. A combination of these techniques can also be used.

Early implementations of non-Cartesian GRAPPA only used k-space segmentation [73,74]. These approaches were limited because large segments had to be used to gather enough kernel instances to estimate the weights, which led to less accurate reconstructions. When collecting instances of the kernel within a segment, an assumption is made that the kernel geometry does not vary over the segment. Therefore, k-space segmentation should be used in moderation as the GRAPPA weights will become less accurate if the segment size is too large and the kernel geometry changes significantly within the segment. The most accurate calibration method is to collect instances of the kernel over several fully-sampled repetitions (through-time calibration), although it may be time-consuming to collect enough repetitions [70]. Because of the tradeoffs between accurate weight estimation and time required to collect enough calibration data, often a combination of small amounts of k-space segmentation and through-time calibration is used.

As an alternative to collecting separate fully-sampled data for calibration, several self-calibrating methods have been developed. These methods use only the accelerated acquisition to estimate the non-Cartesian GRAPPA weights [80–84]. These self-calibrating methods may still use some segmentation in k-space to increase the number of instances of each kernel.

Non-Cartesian GRAPPA algorithms have been developed for various trajectories, including radial [70], variable-density and uniform-density spiral [71,74], rosette [75], and BLADE/PROPELLER trajectories [76,77]. Although more computation is required for non-Cartesian as compared to Cartesian GRAPPA, it is well-suited to parallelization on graphics cards because each target point can be reconstructed independently from other target points. For example, 2D datasets acquired with a radial sampling pattern can be reconstructed into images of matrix size 128×128 using through-time radial GRAPPA in 35 ms [78].

5.3. Non-Cartesian SPIRiT

Unlike SENSE and GRAPPA, it is straightforward to generalize SPIRiT for reconstructing non-Cartesian data. The output of SPIRiT is always a fully-sampled Cartesian k-space, regardless of the original sampling trajectory. The SPIRiT kernel convolutions are performed in the reconstructed Cartesian k-space, and therefore these operations are done as described above. Data consistency is enforced by resampling the Cartesian k-space onto the undersampled non-Cartesian trajectory using convolution interpolation. Ideally the reconstructed (and resampled) k-space should agree with the acquired data at the originally sampled k-space locations.

5.4. Applications of non-Cartesian parallel imaging

Non-Cartesian parallel imaging methods take advantage of efficient use of the gradient coils and incoherent aliasing artifacts to allow potentially higher acceleration factors than Cartesian parallel imaging. However, non-Cartesian methods require more complicated reconstruction schemes and are not used as frequently in non-research settings as their Cartesian counterparts.

A combination of radial sampling, CG SENSE, and compressed sensing called Golden-angle RAdial Sparse Parallel (GRASP) has been demonstrated for contrast-enhanced liver, neck, and breast scans [79]. An extension called XD-GRASP acquires data continuously and reconstructs images corresponding to different motion-resolved states (e.g. different cardiac cycles, respiratory cycles, or stages of contrast enhancement) [80]. SENSE with spiral sampling has been used to accelerate velocity-encoded MRI [81]. Through-time non-Cartesian GRAPPA has been used to collect real-time cardiac data without breathholds or electrocardiogram gating in 45 ms per 2D frame with radial sampling (Fig. 12) [70,82] and 35 ms per frame with spiral sampling [71]. Non-Cartesian GRAPPA has also been applied for renal MRA [72], myocardial [83] and liver perfusion [84], and abdominal T_1 mapping [85]. Late gadolinium enhancement (LGE) cardiac imaging with a 3D spiral trajectory has been accelerated using SPIRiT to enable whole-heart coverage in one breathhold [86]. Radial SPIRiT with compressed sensing has been reported for velocity-encoded MRI [87,88] and real-time imaging of the airway during sleep apnea [89].

In general, non-Cartesian parallel imaging methods require longer reconstruction times than their Cartesian counterparts. One of the most time-consuming steps is the NUFFT, which transforms the non-Cartesian k-space data to the image domain. Processing times are longer for iterative techniques since data are repeatedly transformed between the image domain and k-space. Parallel computing can be harnessed to speed up computation and display images almost immediately after scanning. Such techniques have been explored in research settings for CG SENSE [90], non-Cartesian GRAPPA [78,91], and l_1-SPIRiT [61].

6. Simultaneous multi-slice imaging

The previous sections have described how parallel imaging can be used to reduce the number of phase encoding lines required to generate a 2D image. These methods take advantage of coil sensi-

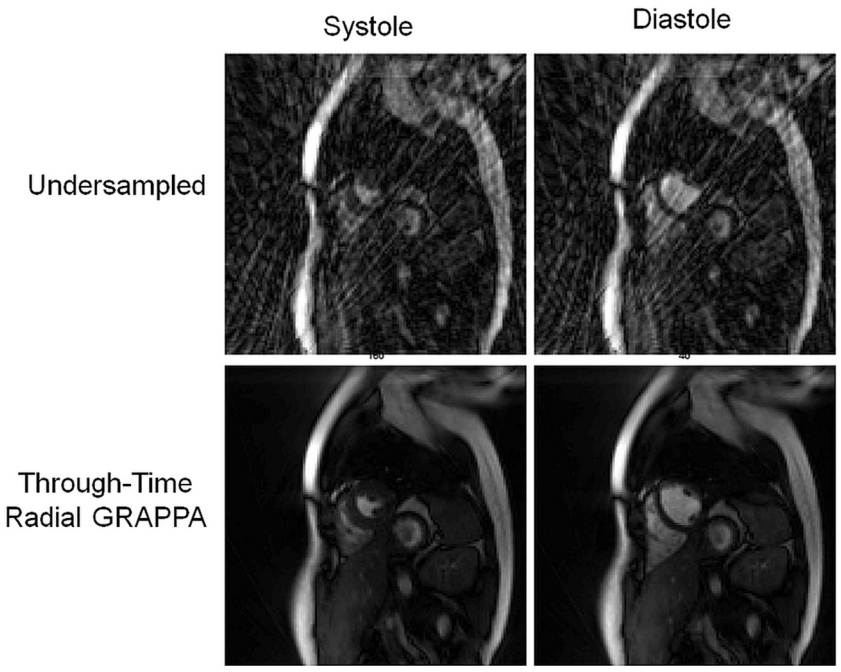

Fig. 12. Representative cardiac images acquired at 3 T with a balanced steady-state free precession sequence in a healthy volunteer and reconstructed with through-time radial GRAPPA. Images were collected during free-breathing without ECG gating. Data were accelerated by a factor R = 9 (16 out of 144 projections), and through-time GRAPPA was applied using 80 calibration frames and an 8 × 4 k-space segmentation (readout × projection). For comparison, the undersampled data were also gridded without reconstruction to show the appearance of streak artifacts. Scan parameters: 128 × 128 matrix, 300 mm^2 FOV, TR = 2.94 ms, flip angle 45°, temporal resolution 47 ms/frame.

tivity variations within the scan plane. However, parallel imaging can also be used to disentangle aliased slices, so that several slices can be imaged during the time it conventionally takes to acquire one slice. These Simultaneous Multi-Slice (SMS) techniques exploit differences in coil sensitivity across the slice-encoding direction but are still grounded in the same parallel imaging principles.

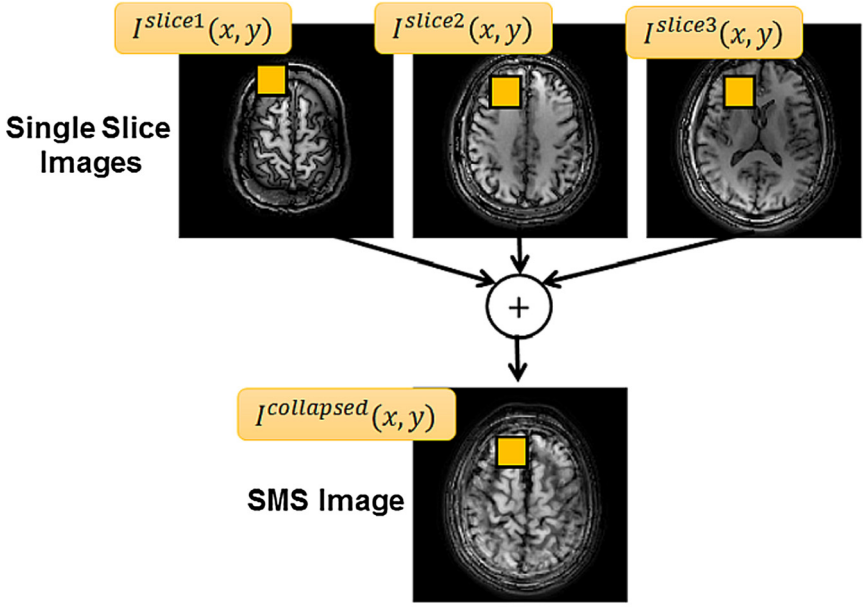

$$\begin{bmatrix} I_1^{collapsed}(x,y) \\ I_2^{collapsed}(x,y) \\ I_3^{collapsed}(x,y) \\ I_4^{collapsed}(x,y) \end{bmatrix} = \begin{bmatrix} S_1^{slice1}(x,y) & S_1^{slice2}(x,y) & S_1^{slice3}(x,y) \\ S_2^{slice1}(x,y) & S_2^{slice2}(x,y) & S_2^{slice3}(x,y) \\ S_3^{slice1}(x,y) & S_3^{slice2}(x,y) & S_3^{slice3}(x,y) \\ S_4^{slice1}(x,y) & S_4^{slice2}(x,y) & S_4^{slice3}(x,y) \end{bmatrix} \begin{bmatrix} I^{slice1}(x,y) \\ I^{slice2}(x,y) \\ I^{slice3}(x,y) \\ I^{slice4}(x,y) \end{bmatrix}$$

Fig. 13. Diagram of a slice-SENSE reconstruction for a multiband factor of MB = 3 with four receiver coils. Signals at the same (x,y) position from all three slices are collapsed in the SMS image. However, because data are acquired with four coils, a SENSE matrix equation can be written to solve for the unknown pixel intensity in each slice, namely $I^{slice1}(x,y)$, $I^{slice2}(x,y)$, and $I^{slice3}(x,y)$.

SMS techniques excite several slices concurrently using multiband radiofrequency pulses [92,93]. Analogous to the acceleration factor, the number of slices acquired simultaneously is called the multiband factor (MB). Multiband pulses consist of a sum of RF waveforms that are each centered on a different frequency band. The composite pulse is applied along with a slice-select gradient to excite spins across multiple frequency bands and hence multiple slices. Care needs to be taken to avoid exceeding specific absorption rate (SAR) restrictions or voltage limits on the RF amplifier. SAR can be a concern when combining SMS with high-energy pulse sequences like spin echo. More advanced multiband pulses, such as VERSE [94], PINS [95], or multi-PINS [96], can be used to reduce RF energy deposition.

SMS techniques have several advantages. The most obvious benefit is a reduction in total scan time, which is especially important for lengthy acquisitions like diffusion tensor imaging or volumetric T_2-weighted scans [97,98]. Whereas conventional parallel imaging has an unavoidable SNR loss, the SNR in SMS scans increases by the square root of the number of slices. Additionally, slice acceleration and in-plane acceleration have different consequences for sequences that acquire multiple phase encoding lines after each RF excitation, like EPI and turbo spin echo (TSE). In-plane acceleration shortens the echo train length by collecting fewer k-space lines, which reduces geometric distortion and blurring from T_2 or T_2^* decay. SMS techniques, on the other hand, decrease the total scan time by acquiring data from several slices in one TR; however, the sequence parameters remain the same with no effect on blurring or distortion. SMS imaging has driven new developments in RF pulse designs that have resulted in less tissue heating [95,96]. SMS is also useful in time-resolved applications like fMRI, where dynamic brain processes can be probed at faster temporal resolutions or with higher SNR [99–101].

6.1. A simple SMS SENSE example

The slice-collapsed SMS data acquired by the scanner are a sum of the signals arising from each slice. Images for each slice can be separated using a standard SENSE reconstruction assuming there are sufficient coil sensitivity differences between slices (Fig. 13) [92]. A reference scan must be acquired for each slice to determine the coil sensitivity profiles. For each pixel in the slice-collapsed image, a sensitivity matrix S of size $n_S \times n_C$ is formed, where n_S and n_C are the number of slices and coils, respectively. As described in the SENSE section, the reconstruction is expressed as

$$\boldsymbol{v} = (S^H S)^{-1} S^H \boldsymbol{a} \tag{11}$$

where $\boldsymbol{v}$ contains the unfolded pixels for each slice with size $n_S \times 1$, and $\boldsymbol{a}$ contains the signals at a given pixel location in the slice-collapsed data with size $n_C \times 1$.

In practice, this simple SENSE reconstruction may result in enhanced noise or residual slice aliasing. One reason for these errors is that the adjacent slices may be close together in space (on the order of tens of millimeters) so that the coil sensitivities of the two slices are nearly identical, making the inversion highly ill-conditioned. A second reason is that many coil arrays have less encoding power along the slice direction with standard coil geometries. Thus, alternative SMS parallel imaging methods have been investigated.

6.2. Multi-Slice CAIPIRINHA

In multi-slice (MS-)CAIPIRINHA, the aliasing of the collapsed slices is modified to make better use of coil sensitivity differences [102]. In the previous example using SENSE (illustrated in Fig. 14a), signals from each slice are superimposed directly on top of each other. Parallel imaging methods can only exploit coil sensitivity variations along the slice-encoding direction, which may be minimal. With MS-CAIPIRINHA, signals are still summed over all slices, but each slice is also shifted within the imaging plane (Fig. 14b). MS-CAIPIRINHA thus makes use of sensitivity differences along both slice and phase-encoding directions to separate slices more easily.

The in-plane shifts in MS-CAIPIRINHA are made possible through the Fourier Shift Theorem, which states that a translation

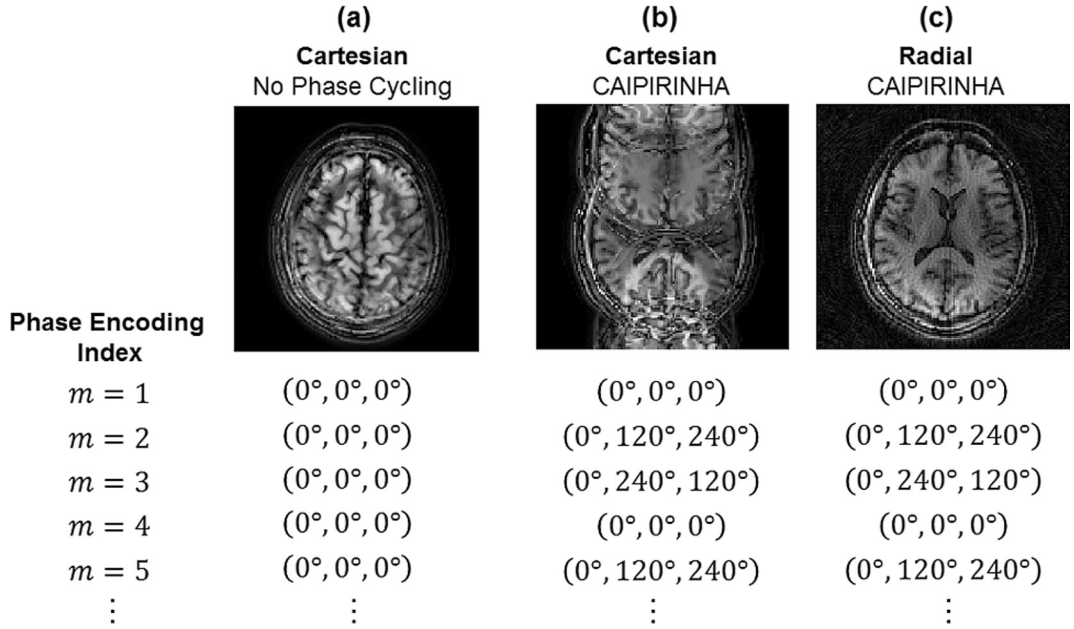

Fig. 14. Examples of slice-collapsed SMS images with MB = 3 acquired with three different sampling schemes. (a) Cartesian k-space sampling where all RF pulses have zero-degree phase results in coherent slice aliasing. (b) Cartesian k-space sampling with CAIPIRINHA RF phase cycling shifts each slice within the FOV so they do not lie directly on top of one another. (c) Radial k-space sampling with CAIPIRINHA phase cycling causes signals from one slice to add coherently, while signals from other slices add destructively and appear as background noise or streak artifacts.

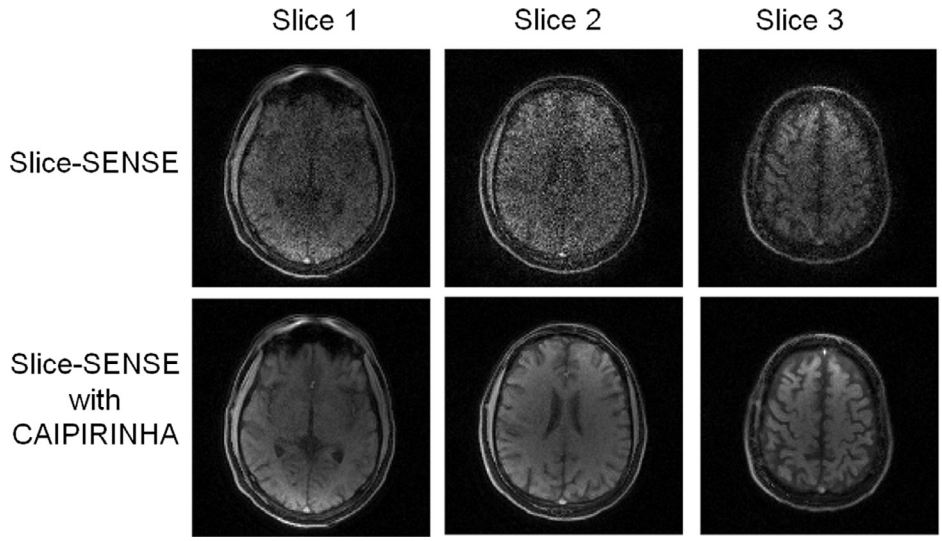

Fig. 15. Representative images from an SMS brain scan acquired with multiband factor MB = 3 (5 mm slice thickness, 30 mm slice gap) at 3 T with a 32-channel brain array. Data were reconstructed using slice-SENSE. Reference scans for each slice were acquired separately to estimate the coil sensitivities. (Top row) Images reconstructed without RF phase cycling show severe noise enhancement. (Bottom row) Data sampled using CAIPIRINHA RF phase cycling to shift the aliased slices within the FOV have less noise enhancement.

in the image domain is equivalent to a multiplication of the k-space signals by a linear phase

$$\rho(y-\Delta y)=\sum_{m=-\frac{N}{2}}^{\frac{N}{2}} S(m\Delta k)e^{im(\Delta k)(y-\Delta y)} \tag{12}$$

$$\Delta k=\frac{2\pi}{FOV} \tag{13}$$

In these equations, m is the phase encoding index which varies between $-N/2$ and $N/2$, and Δy is the number of pixels by which the image is shifted. In Fig. 14b, slice 1 has zero shift, slice 2 is shifted by $FOV/3$ pixels, and slice 3 is shifted by $2/3 * FOV$ pixels.

One way to implement in-plane shifts is using RF phase cycling. Each phase encoding line in k-space for a Cartesian scan is given a unique RF phase. Recall that multiband pulses are the sum of simpler, single-band RF waveforms. The RF waveform for each slice is modulated by a certain phase before the waveforms are added together to create the multiband pulse. Fig. 14b shows an example of RF phase cycling for a multiband factor of 3. This type of phase cycling pattern was originally reported in a technique called POMP [103] and can be generalized for any multiband factor. POMP-like phase cycling will shift the slices in the collapsed image equidistantly across the FOV. For a dataset with n_S slices, the RF phase modulation for the m^{th} phase encoding step and slice l is

$$\phi(l,m)=\frac{(l-1)(m-1)FOV}{n_s} \tag{14}$$

It is not straightforward to apply MS-CAIPIRINHA to sequences that already modify the RF phase. For example, balanced steady-state free precession (bSSFP) sequences maintain steady-state conditions by alternating the RF phase between 0 ° and 180 ° between each TR. Rather than using the POMP-like phase cycles described above, linear RF phase cycles are applied to both maintain steady-state and shift each slice in the FOV [104]. Sequences that read out multiple k-space lines after each excitation are also incompatible with RF phase cycling to shift the aliased slices. Instead, blipped CAIPIRINHA applies small gradient blips on the slice-select axis to produce a phase difference between slices [105]. Unlike an early implementation of this method [106], the blips alternate in polarity to avoid phase buildup during the EPI readout, which would otherwise lead to signal attenuation with longer readouts.

Single slice images can be reconstructed using SENSE with slight modifications to account for the shifted aliasing pattern. Compared to the non-shifted SMS acquisitions, MS-CAIPIRINHA results in lower g-factors and higher SNR by making more effective use of 3D coil sensitivity variations. Fig. 15 shows an example of a brain scan acquired with and without MS-CAIPIRINHA and reconstructed using slice-SENSE. The images without MS-CAIPIRINHA are degraded by noise amplification due to the insufficient sensitivity variations along the slice encoding direction.

Although CAIPIRINHA outperforms SMS without phase cycling, Cartesian sampling results in coherent artifacts which can be difficult to completely resolve using parallel imaging. Many non-Cartesian trajectories, like radial and spiral, cross the center of k-space with each excitation. When these sampling patterns are combined with CAIPIRINHA, signals from one slice add coherently, while signals from all other slices add destructively and appear as background noise [107]. There is less aliasing energy in the slice-collapsed data, which puts less strain on the parallel imaging reconstruction. Fig. 14c shows an example of an SMS experiment with radial sampling and a multiband factor of 3. The raw slice-collapsed image only contains coherent signals from slice 1, while the other two slices appear as incoherent background noise and streak artifacts. Since the RF phase pattern is user-defined, an image containing coherent signal from only slice 2 (or slice 3) can be created by multiplying the SMS k-space data by the complex conjugate phase pattern for slice 2 (or slice 3). This simple conjugate phase reconstruction does not completely remove the artifacts from other slices, which can be addressed using a modified CG SENSE algorithm.

6.3. GRAPPA methods for SMS imaging

Several variants of GRAPPA have been developed for SMS imaging. One of the first techniques, termed SENSE-GRAPPA, was originally used for reconstructing 3D datasets with undersampling along both phase and partition encoding directions [108]. Low-resolution ACS images are acquired separately for each slice, and

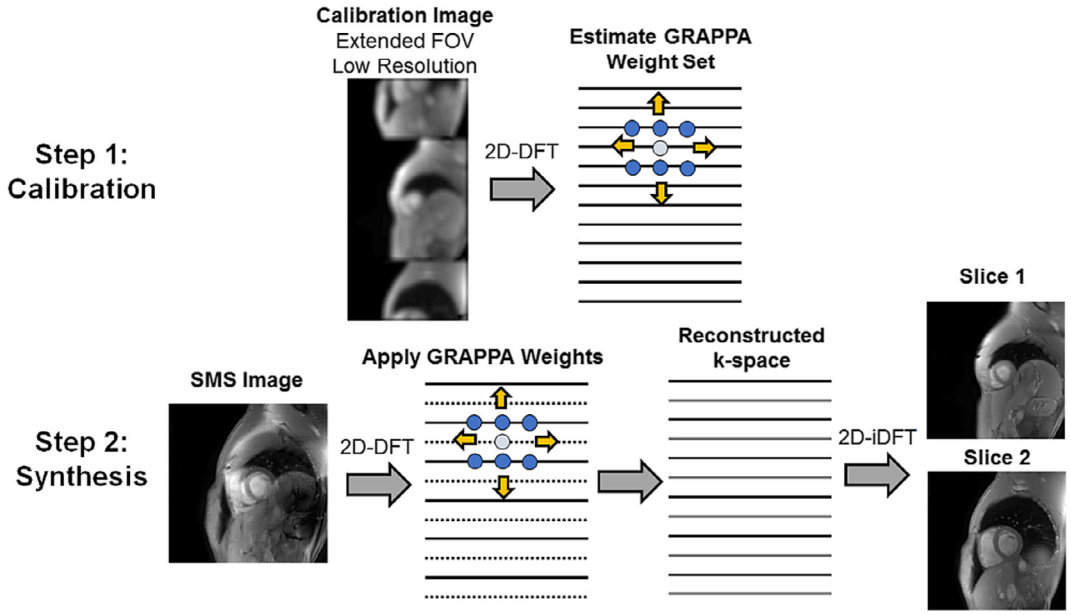

Fig. 16. Overview of SENSE-GRAPPA for SMS imaging. First, low-resolution prescans are acquired for each slice separately. The images are concatenated to create an extended FOV image. After applying a 2D-DFT, a GRAPPA weight set is estimated using these data. Next, the slice-collapsed SMS image is transformed to k-space in a similar fashion. A standard 1D GRAPPA reconstruction is performed, and an inverse 2D-DFT is applied to yield an image containing the two separated slices.

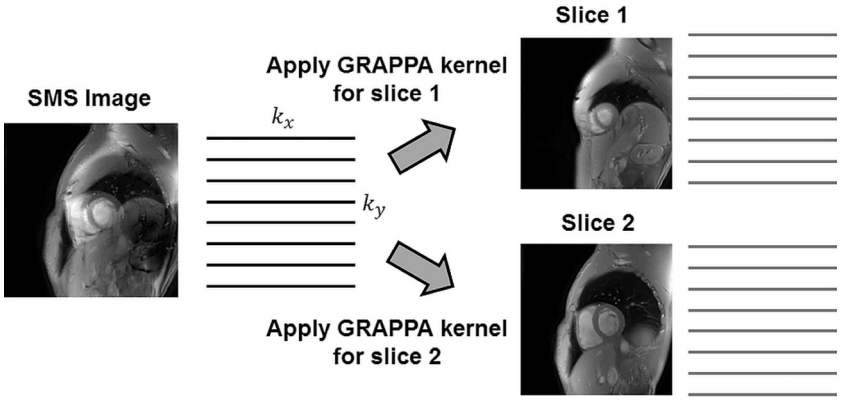

Fig. 17. Schematic of a slice-GRAPPA reconstruction for SMS imaging. First, low-resolution calibration scans are collected individually for each slice. A different GRAPPA kernel is estimated for each slice and applied to the SMS k-space to synthesize an entirely new k-space for each slice.

they are concatenated in the image domain to create a 2D matrix with an extended FOV along the phase encoding direction (Fig. 16). The image data are transformed into a virtual ACS for estimating the GRAPPA weight set. Next, the slice-collapsed images are concatenated in a similar fashion, and a conventional GRAPPA reconstruction separates the individual slices. As described in the GRAPPA section, the calibration and SMS scans may be acquired with different sequence parameters without affecting the stability of the GRAPPA weights. SENSE-GRAPPA can be used to reconstruct both in-plane and slice acceleration in a single step. However, residual aliasing or discontinuities may occur for certain acceleration and multiband factors. With CAIPIRINHA acquisitions, sharp high-frequency transitions will exist in the extended FOV image (due to the shifted aliasing pattern) that cannot be synthesized by a GRAPPA kernel. The extended FOV image can be zero-padded to alleviate this problem when combining SENSE-GRAPPA with CAIPIRINHA sampling [105].

In Slice-GRAPPA [105], a separate calibration scan is acquired for each slice and used to estimate a set of slice-specific kernels (Fig. 17). The kernels are applied to the slice-collapsed data to synthesize an entirely new k-space for each slice. This procedure is different from conventional GRAPPA, which only synthesizes missing phase encoding lines. Unlike SENSE-GRAPPA, slice-GRAPPA can only resolve slice aliasing, so a second parallel imaging step is needed to rectify the in-plane aliasing. Despite the similar name, slice-GRAPPA has different properties than conventional GRAPPA. The slice-GRAPPA kernels depend somewhat on the underlying magnetization, so the same sequence parameters and image contrast should be used for calibration and SMS scans. Artifacts may sometimes be hard to interpret; since slices are calibrated and reconstructed independently, residual aliasing may appear in some slices but not others.

Analogous to the g-factor for conventional parallel imaging, the amount of residual slice aliasing can be quantified using the slice leakage artifact or L-factor [109]. For slice-GRAPPA, the L-factor can be calculated analytically from the GRAPPA weights. Split slice-GRAPPA uses the L-factor to optimize the weight calibration to trade off slice leakage and in-plane artifacts [110].

6.4. Applications of SMS imaging

While some vendors do support SMS imaging for clinical use, many techniques are still mainly used in research settings. Neuroimaging is the most common application for SMS imaging, especially for diffusion-weighting imaging and fMRI [99]. For instance, whole-brain fMRI scans can be performed in less than 200 ms per volume using blipped CAIPIRINHA with spiral trajectories [101], and more information can be gleaned from the blood oxygenation level dependent (BOLD) signal at such high temporal resolutions [111]. In body imaging, SMS has been applied to diffusion imaging of the breast [112], real-time cardiac CINE [104] and first-pass myocardial perfusion imaging [113,114], and real-time monitoring of airway collapse during sleep apnea [115]. Imaging and navigator slices for free-breathing abdominal imaging can be collected simultaneously using SMS [116]. Multiple slices with different RF phase cycling patterns can be acquired to reduce banding artifacts in balanced steady-state free precession sequences [117].

7. 3D parallel imaging

Many of the techniques discussed previously have been generalized for accelerated 3D imaging. Some distinctions should be made between multi-slice and 3D MRI. In multi-slice imaging, a stack of thin 2D slices separated by gaps is collected; only one direction is phase encoded, and each slice is reconstructed using a 2D DFT. Multiple slices can be acquired sequentially, in an interleaved manner, or simultaneously using SMS techniques. In contrast, a thick slab of tissue is excited in 3D imaging. Spatial encoding is performed using phase encoding gradients along two spatial dimensions, and images are reconstructed using a 3D DFT. Because a full 3D k-space is collected, the acquisition time is prolonged according to

$$TA = TR \cdot N_y \cdot N_z \cdot N_A \tag{15}$$

where N_y is the number of phase encoding steps along k_y, N_z is the number of partition encoding steps along k_z, and N_A is the number of signal averages (which typically equals one for many imaging applications).

The decision of whether to use multi-slice or 3D imaging depends on the clinical application. Three-dimensional imaging can have different artifact properties compared to single-slice imaging. For example, k-space inconsistencies due to motion will corrupt the entire 3D volume, whereas the 2D slices in an SMS scan can be acquired more quickly and are less likely to be corrupted by motion. SMS scans require specialized radiofrequency pulses that are not needed for 3D imaging. Because SNR is proportional to the volume of excited spins, 3D imaging (like SMS) has high SNR that can partially offset the SNR loss due to parallel imaging. Additionally, coil sensitivity variations can be harnessed along all three directions. For 2D Cartesian scans with acceleration along one direction, noise enhancement and residual aliasing tend to appear above acceleration factors of 3 or 4 for most coil arrays. The net acceleration factor for a 3D scan is the product of the acceleration factors along each direction. Therefore, high total acceleration factors can be attained by combining a modest amount of undersampling along each direction.

In broad terms, 3D trajectories can be classified as 3D Cartesian, 3D cylindrical (where the k_x - k_y plane is sampled in a non-Cartesian fashion but k_z is sampled along a Cartesian grid), and 3D spherical (where all points are sampled on a non-Cartesian grid). Both partition encoding and phase encoding lines (or non-Cartesian projections) can be skipped to reduce scan time, and then subsequently reconstructed with parallel imaging.

7.1. 3D SENSE, GRAPPA, and SPIRiT

2D SENSE uses coil sensitivity information to unfold aliased pixels in a 3D volume (it is called "2D SENSE" because both phase encoding directions may be subsampled) [118]. Prior to reconstruction, an additional low-resolution coil sensitivity map is obtained covering the whole volume. The sensitivity matrix can be written the same way as for the 2D case using knowledge of the undersampling pattern. For 3D Cartesian undersampling, the SENSE reconstruction can be implemented with simple matrix inversions, while iterative methods like CG SENSE are used for 3D non-Cartesian data.

Several approaches to 3D GRAPPA have been published. One method, called 2D GRAPPA, uses a three-dimensional GRAPPA kernel (Fig. 18) [119]. One target point in a single coil is synthesized as a weighted sum of source points from all coils in a surrounding 3D neighborhood. Calibration data are acquired as a contiguous 3D block near the center of k-space. A second approach is to use a 1D GRAPPA operator method that sequentially reconstructs each undersampled dimension with a two-dimensional GRAPPA kernel. In such a reconstruction it is possible to tailor the calibration scan by acquiring two sets of reference data for estimating each set of GRAPPA weights independently. The 1D GRAPPA operator may result in better image quality because the weight matrices are less susceptible to motion and better determined—i.e. the three-dimensional kernel has more source points than the two-dimensional kernel, and thus is less overdetermined for a given

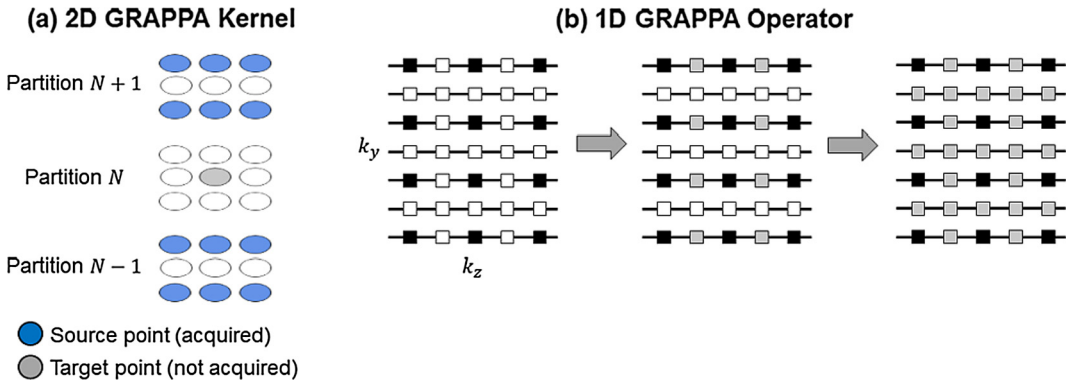

Fig. 18. Two approaches using GRAPPA to reconstruct 3D datasets with undersampling along phase and partition encoding directions. (a) In 2D GRAPPA, each target point is synthesized using a three-dimensional kernel with source points taken from a 3D neighborhood. (b) In the 1D GRAPPA operator approach, each subsampled dimension is reconstructed in a separate step using a two-dimensional kernel. In this diagram, missing partitions (white dots) are reconstructed first (gray dots); missing phase encode data are reconstructed in the second step. Acquired data points are shown in black, and the readout dimension (k_x) is not illustrated for simplicity.

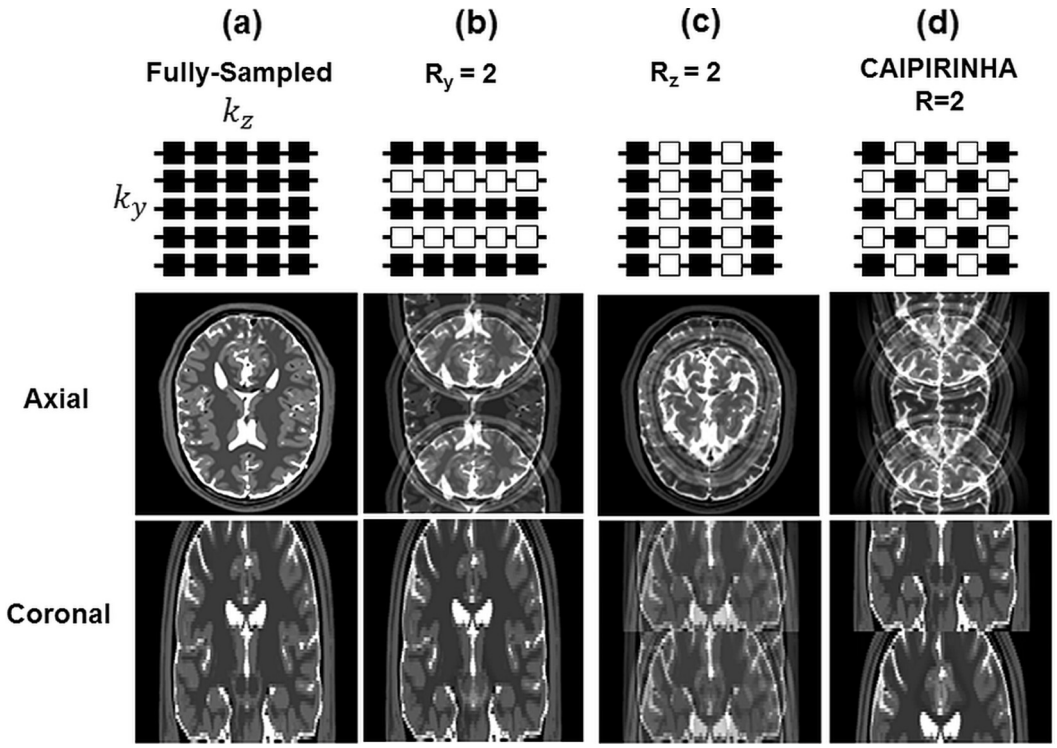

Fig. 19. Comparison of standard 3D Cartesian undersampling versus CAIPIRINHA. For simplicity, the readout dimension (k_x) is not illustrated. (a) Fully-sampled images are shown for reference in axial and coronal views. (b) R = 2 undersampling along k_y produces foldover artifacts along the y-direction. (c) R = 2 undersampling along k_z causes two partitions to fold onto each other. (d) With R = 2 CAIPIRINHA undersampling, the k-space sampling pattern is staggered. Two partitions still fold onto each other, but the images are also shifted by half the FOV, making them easier to unfold.

amount of calibration data. However, the sequential nature of the application of the two sets of GRAPPA weights may lead to error propagation in the 1D GRAPPA operator approach which is not seen in 2D GRAPPA.

SPIRiT and related methods can also be generalized for 3D imaging. In this case, a SPIRiT kernel is employed that synthesizes each 3D Cartesian k-space point as a weighted sum of grid points in a surrounding 3D neighborhood. Likewise, data consistency is performed using a 3D NUFFT operation.

7.2. 2D CAIPIRINHA

High net acceleration factors can be achieved by splitting the undersampling along both phase encoding dimensions in a 3D scan, which better exploits the differences in coil sensitivities across the whole volume. 2D CAIPIRINHA takes this idea further by shifting the k-space points from a standard rectangular grid onto a sheared lattice [120]. This shift modifies the aliasing pattern thereby leading to more robust parallel imaging reconstructions. Note that 2D CAIPIRINHA is an extension of MS-CAIPIRINHA for 3D MRI.

In Fig. 19, several 3D undersampling strategies are compared. For the case of R = 2 along k_y, two equally spaced pixels along the y-direction fold on top of each other in the aliased image. Likewise, for R = 2 along k_z, two pixels along the partition direction are superimposed. However, if the coil array does not have sufficient encoding power along the accelerated direction, it will not be possible to separate the aliased pixels. One solution is to divide the acceleration equally along both dimensions using an R = 2 CAIPIRINHA pattern, where the sampled points are offset from one phase encoding line to the next. The two partitions still fold on top of one another, but the aliased pixels are also shifted within each partition.

Unlike MS-CAIPIRINHA, 2D CAIPIRINHA does not require special hardware or RF pulses. The shifted k-space sampling is implemented by simply adjusting the phase and partition encoding gradients. Undersampled data can be reconstructed using standard SENSE, GRAPPA, or SPIRiT with slight modifications to account for the offset sampling.

Some research has been devoted to choosing an optimal CAIPIRINHA sampling pattern, which depends on scan-specific variables including coil configuration, coil loading, and FOV [121]. Some strategies for determining the best CAIPIRINHA shifts are to create a g-factor map from a low-resolution reference scan or to perform a principal component analysis of the coil sensitivities. Optimal patterns tend to maximize the distance between aliased pixels, as distant pixels often experience more differences in coil sensitivities than nearby pixels.

Several clinical applications of 2D CAIPIRINHA have been investigated. Breath-held liver scans with Cartesian CAIPIRINHA (R = 2 × 2 in phase and partition encoding directions) can produce similar image quality as R = 2 with standard GRAPPA [122]. In DCE exams, CAIPIRINHA can improve the temporal resolution to capture arterial enhancement in breath-held scans of the liver [123,124] and pancreas [125]. CAIPIRINHA can be combined with view-sharing and Dixon water-fat separation to produce fat-only and water-only images of the liver [126]. High-resolution 3D knee images can be acquired in under 5 min using CAIPIRINHA [127].

7.3. Wave CAIPIRINHA

Most 3D parallel imaging techniques only exploit coil sensitivity variations along the phase and partition encoding directions and ignore variations along the readout dimension. However, wave CAIPIRINHA samples k-space along a trajectory that can take full advantage of 3D coil sensitivity differences [128]. Data are

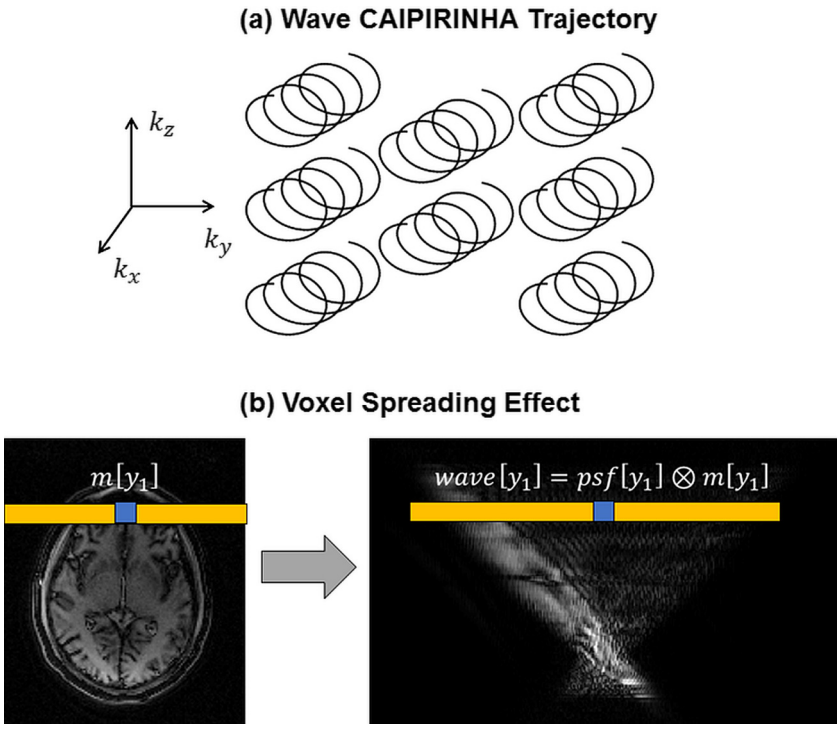

Fig. 20. Diagram of Wave CAIPIRINHA for 3D MRI. (a) Each non-Cartesian readout is a corkscrew along the k_x axis, and multiple corkscrew trajectories are staggered throughout the 3D k-space using CAIPIRINHA sampling. (b) The wave trajectory spreads the signal from one voxel across an entire row. As shown in the equation, this process is modeled as convolving the magnetization at one point by a point spread function. When data are undersampled, signal from one point in the image is spread over multiple rows.

acquired using a 2D CAIPIRINHA sampling pattern so that signals from aliased partitions are shifted with respect to each other. In addition, sinusoidal gradients along y and z are applied during the readout. The net effect is a trajectory that winds along k_x like a corkscrew (Fig. 20). Because of the CAIPIRINHA sampling, multiple corkscrew trajectories are staggered in 3D k-space, and aliasing energy is spread in three dimensions.

Although the wave trajectory is non-Cartesian, it has the unusual property that images can be generated using DFT operations without gridding or the non-uniform FFT. Images are reconstructed by deconvolving the data with a point spread function (PSF), which can be visualized by taking a DFT along the readout direction. The sinusoidal gradients impose a phase in k-space, which leads to a PSF that depends spatially on y and z. More blurring is induced at rows farther from the center of the imaging volume. As shown in Fig. 20b, signal from one voxel will be blurred across its entire row (note that only the sinusoidal y-gradient is considered, and the z-gradient is assumed to be zero for simplicity). In an example with R = 2 undersampling in-plane, signal from one voxel will be blurred across two rows. In other words, two entire rows of pixels are aliased instead of two individual pixels. The blurring increases the distance between folded pixels, which is beneficial for parallel imaging. The reconstruction is more complex than this simple example because there is voxel spreading across both y and z directions, and the aliasing pattern is shifted using 2D CAIPIRINHA. After accounting for these effects, the undersampled data are reconstructed using a SENSE model. Like Cartesian SENSE, the encoding matrix is small and can be solved efficiently and in parallel.

Because Wave CAIPIRINHA makes use of the full 3D coil sensitivities, it can be used to achieve high acceleration factors with small g-factor penalties and less SNR degradation. Results have been demonstrated with $R = 3 \times 3$ (along phase and partition encoding directions) to achieve whole-brain 1 mm^3 isotropic resolution in slightly over two minutes at 7 T [128].

8. Phase-constrained parallel imaging

The next section focuses on another branch of reconstruction methods known as phase-constrained parallel imaging. MR images have both magnitude and phase, and these techniques use knowledge of the object phase to complement the spatial encoding provided by gradients and coil arrays. Phase-constrained methods can sometimes achieve higher acceleration factors or exhibit less noise enhancement compared to similar methods that do not incorporate phase. Inherent background phase exists from the receiver coil phase profile, B_0 field inhomogeneities, and many other sources [129]. The following sections will briefly summarize several of these techniques including phase-constrained SENSE, virtual conjugate coil methods, P-LORAKS, and phase-constrained SMS imaging.

8.1. Phase-constrained SENSE

Conventionally in SENSE, the unknown variables are complex-valued pixel intensities. Phase-constrained SENSE (PC-SENSE) instead assumes that the magnetization is real-valued, which reduces the number of variables by half [129,130]. This improves the conditioning of the sensitivity matrix so it is more easily inverted, and it decreases the overall g-factor. PC-SENSE requires a prescan to determine both the receive coil profiles and the background phase distribution; these are lumped into one quantity called the effective coil sensitivities. The prescans are typically acquired at low resolution to decrease scan time. PC-SENSE is prone to errors if there are high frequency phase variations that are not captured in the prescan. Such phase discontinuities can occur near air-tissue boundaries, in fatty tissues, or around blood vessels. The phase constraints may be regularized to decrease artifacts at the expense of lower SNR [131], or high-resolution phase

maps may be recovered iteratively and then used to reduce artifacts [132].

8.2. Virtual conjugate coils

In general, the performance of a parallel imaging reconstruction improves with higher coil counts. The number of channels can be artificially increased (as much as doubled) by creating "virtual coils" [133]. Virtual coils are generated by taking the complex conjugate of signals in k-space from actual physical coils

$$S_{j+n_C}(k) = S_j^*(-k) \tag{16}$$

where j is the coil index and n_C is the number of physical coils. Because the effective coil sensitivities are complex, the virtual coils contain different information and hence improve the reconstruction.

In virtual conjugate coil SENSE (VCC-SENSE), the sensitivity matrix is populated using the physical and virtual coils, and the magnetization is assumed to be real. Rather than reducing the number of variables like PC-SENSE, VCC-SENSE doubles the number of equations, leading to a more overdetermined system. VCC-SENSE is mathematically equivalent to PC-SENSE.

Virtual coils can also be applied to k-space-based reconstructions. Virtual k-space signals are created for both ACS and undersampled data points, which are then used in a standard GRAPPA, SPIRiT, or ESPIRiT reconstruction. On the one hand, the virtual coils improve the reconstruction quality by providing additional sensitivity information; however, the GRAPPA or SPIRiT weights require additional data for the calibration equations to be fully determined. The k-space methods have the advantage of not requiring explicit estimates of the coil sensitivities or background phase. Unlike PC-SENSE, the reconstructed images are not real-valued but contain both magnitude and phase information. The k-space reconstructions also tend to be robust in the presence of high-frequency phase variations. Unlike conventional GRAPPA or SPIRiT, the calibration and undersampled data should be collected with the same sequence parameters so the object phase is consistent.

8.3. LORAKS

Low-rank modeling of local k-space neighborhoods (LORAKS) works by reconstructing k-space data using low rank matrix completion [134,135]. The reconstruction attempts to find a solution that is both consistent with the undersampled data and also satisfies two special properties. When these properties are satisfied, then matrices constructed from k-space kernel operations will have low rank (i.e. only a small number of linearly independent rows or columns) because nearby k-space data points will be correlated. The first property assumes that the image has limited support, meaning that there are background pixels which contribute no signal. Second, the image is assumed to have smooth, slowly varying phase. LORAKS operates on single-channel data and hence is not a parallel imaging method. However, P-LORAKS implicitly uses coil sensitivity information by incorporating k-space data from all channels [136]. The support condition is improved because the uncombined coil images are localized in space. In addition, P-LORAKS incorporates ideas from GRAPPA that each k-space point can be expressed as a weighted sum of nearby acquired points. Fig. 21 shows in more detail how the image support and phase constraints in P-LORAKS are connected to low rank matrices. Another extension of LORAKS is SENSE-LORAKS [137], which includes a SENSE forward model in the data consistency term.

LORAKS and related methods have the advantage of not requiring calibration data. They are compatible with non-uniform k-space trajectories which are challenging for many other parallel imaging techniques, such as random undersampling with partial Fourier reconstruction.

8.4. Imposing a background phase distribution

The background phase can be manipulated to improve the performance of phase-constrained reconstructions. One approach is to offset the k-space sampling by some amount Δk [138], which will impart a phase ramp across the image per the Fourier Shift Theorem. It has also been proposed to use spatially selective RF pulses to tailor the phase distribution [139]. Another technique adjusts the shim to impose a quadratic background phase, which is used

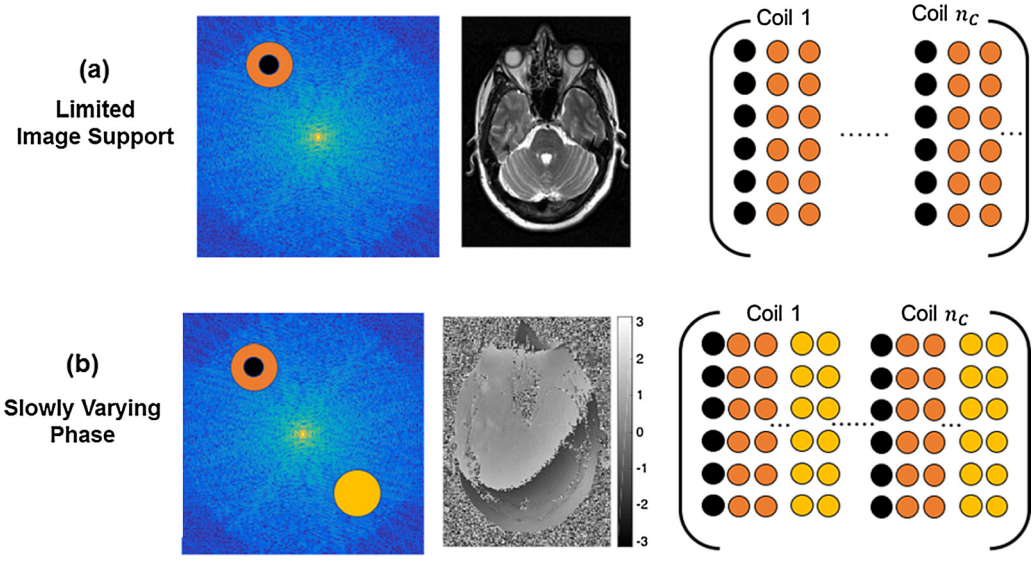

Fig. 21. Two of the key regularization terms used in LORAKS. (a) Multichannel data have limited support in the image domain because the coil sensitivities are localized in space. The LORAKS support matrix is created by extracting a neighborhood around each k-space point (over all coils) and reshaping the data to populate a row in the matrix. The support matrix should have low rank (i.e. only a few independent rows). (b) MR images tend to have slowly varying phase, as seen in this brain scan. The reconstruction creates a matrix using k-space points in an immediate neighborhood, as well as the complex conjugate data from a distant neighborhood. This matrix should have low rank provided the phase variations are smooth. LORAKS finds an optimal solution that satisfies the low rank conditions and is also consistent with the acquired data.

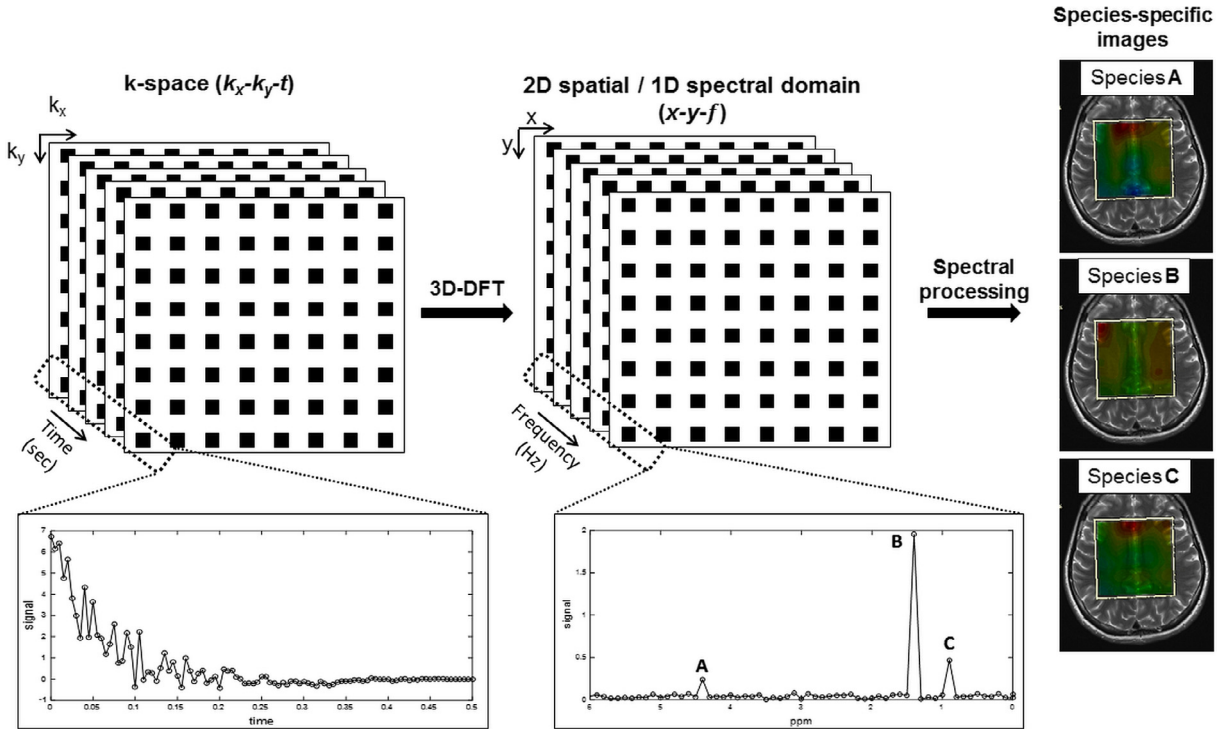

Fig. 22. Schematic of an MR spectroscopic imaging experiment with two spatial dimensions and one spectral dimension. (Left) Raw data are acquired in a k_x-k_y-t space. (Middle) A 3D Fourier Transform converts the k-space signals to x-y-*f* space, or the spatial/spectral domain, which represents the chemical shift spectrum of each voxel in the object. (Right) The spectra can be processed to yield individual maps displaying the spatial distribution of each chemical species. Red indicates a higher concentration of the given metabolite, while blue and green indicate lower concentrations. (For interpretation of the references to color in this figure legend, the reader is referred to the web version of this article.)

to derive coil sensitivities or ACS lines for a subsequent SENSE or GRAPPA reconstruction [140]. In theory, the optimal phase distribution for a given scan orientation and coil setup could be computed by minimizing the g-factor.

8.5. Phase-constrained SMS imaging

Phase-constrained imaging can provide better slice separation when using an SMS reconstruction. Even without parallel imaging, two collapsed slices can (in theory) be perfectly separated using a dualband RF pulse with a 90-degree phase difference between the slices [133]. In one parallel imaging technique, a constant and unique phase offset is applied to each slice, and the SMS images are separated using SENSE-GRAPPA [141]. The optimal phase difference depends on many factors, including the coil configuration and background phase. LORAKS has also been applied to SMS imaging [142]. Data consistency is enforced by adding the reconstructed k-space signals over all slices and comparing the result with the acquired slice-collapsed data, and the LORAKS regularization terms are summed over all slices. SMS-LORAKS is noteworthy because it can handle non-standard or pseudorandom phase cycling schemes besides the standard POMP-like phase cycles, which spread the aliasing energy more evenly through the FOV.

9. Magnetic resonance spectroscopic imaging

MR Spectroscopic Imaging (MRSI), also known as Chemical Shift Imaging (CSI), refers to the localization of different, heterogeneously-distributed chemical species over an object. Compared to traditional spectroscopy, in which the spectral content of a bulk sample is assessed, MRSI uses spatial encoding gradients to obtain individual spectra from several voxels over the object. Alternatively, MRSI can be thought of as the addition of a spectral dimension to an MRI experiment. For simplicity, a 2D spatial/1D spectral case will be described, although this can be extended to higher spatial and spectral dimensions.

In the conventional implementation of MRSI (Fig. 22), two phase encoding gradients are applied to spatially encode the object before sampling a free-induction decay (FID), spin echo, or gradient echo in the time domain. From an imaging perspective, the frequency encoding gradient is replaced by the collection of spectral data (where the "frequency encoding" is the chemical shift dimension), and all spatial encoding is performed using phase encoding gradients. The k-space can be considered to have k_x and k_y directions plus an orthogonal time dimension along which the different chemical shift frequencies are sampled. To recover images, a 3D-DFT is applied over the two spatial dimensions to yield a 2D image and over the time dimension to yield a spectral profile for each voxel in the image. The spectra can be further processed to construct separate 2D images that each display the distribution of a different chemical species. A more in-depth review of MRSI is given by [143], while this section focuses primarily on parallel imaging applications.

In conventional MRSI, one k_x-k_y point in k-space is sampled at a time. Compared to a standard imaging experiment acquired with the same matrix size and sequence parameters, the acquisition time for MRSI is significantly longer. For example, with a TR of 1.5 s and matrix size of 32×32, the total acquisition time for an MRSI scan would be $32 \times 32 \times 1.5$ s = 1536 s, or about 25 min, while a standard imaging scan would only require 32×1.5 s = 48 s. The long scan times point to the potential utility of parallel imaging methods.

Several of the parallel imaging methods described above have been applied to MRSI to accelerate the spatial encoding process. In SENSE with MRSI, the phase-encoded spatial dimensions are undersampled, and an unfolding algorithm as described for SENSE

is used to recover unaliased images [144]. Similarly, GRAPPA can be performed over the spatial dimensions, but the process must be repeated for each point sampled over the time dimension [145]. ACS data can be acquired by acquiring fully-sampled data at the center of k-space or by using a separate low-resolution scan. Recently, a feasibility study was performed to evaluate using CAIPIRINHA to accelerate along three spatial dimensions [146]. The method is termed (2 + 1)D CAIPIRINHA to denote 2D-CAIPIRINHA in-plane and MS-CAIPIRINHA along the slice dimension, resulting in a multi-slice acquisition.

Parallel imaging techniques can also be used with other fast MRSI methods, such as spin-echo trains [147], echo-planar spectroscopic imaging (EPSI) [148–151], and spiral k-space trajectories [152,153] to further reduce acquisition time. Note that parallel imaging can only be carried out along dimensions that are phase-encoded. In methods such as Cartesian EPSI, one spatial dimension is frequency-encoded during the readout, and parallel imaging can only be used along the remaining phase-encoded dimensions.

Another category of spatially localized spectroscopic techniques is single-voxel spectroscopy (SV-MRS). Signal is acquired from a single voxel using three RF pulses to excite three orthogonal slices, with the voxel located at their point of intersection. STEAM (stimulated echo acquisition mode) [154] and PRESS (point resolved spectroscopy) [155] are two common methods of applying the pulses to receive a stimulated echo (STEAM) or a spin echo (PRESS) from the selected voxel. This process can be repeated for several voxels to obtain localized information for clinical use. However, data collection can be time-consuming, and such an analysis is only performed for a small number of positions. Accelerated multivoxel spectroscopy using parallel imaging [156] was recently introduced as a possible method to speed up acquisition. Like simultaneous multi-slice methods described above, simultaneous excitation with a multiband RF pulse is used to excite more than one voxel at a time, and receiver coil sensitivity profiles are used to separate the signals from different voxels.

Parallel imaging has been shown to offer significant acceleration for MRSI, especially when combined with other fast imaging techniques. GRAPPA with EPSI can be used to reduce acquisition of 2D brain data (matrix size 32×32, voxel size 1.9 cm^3) at 3 T from 64 s to 16 s [150]. At 7 T in the brain, both SENSE and GRAPPA have been used to reduce acquisition times from over 50 min to under 13 min (matrix size 29×27, voxel size 0.74 cm^3) [157], and from approximately 65 min to about 8 min (matrix size 64×64, voxel size $3.4 \times 3.4 \times 10$ mm^3) [158].

Parallel imaging may also be promising for accelerating hyperpolarized ^{13}C MRSI, which can be used to investigate metabolic pathways in real time to explore, for instance, altered pathways in cancer [159,160]. SENSE has been used to reduce 2D acquisition from 43 s to 14 s [161], and parallel imaging with EPSI has been used to collect 3D pyruvate and lactate images from rat kidneys in a few seconds [162].

Parallel imaging in MRSI has primarily been performed in phantoms, animal studies, and healthy volunteers to demonstrate the feasibility of different methods. As with other parallel imaging methods, it is important to consider SNR losses due to undersampling and g-factor effects [163]. Reduced SNR can be a greater concern in MRSI compared to MRI due to the inherently low signal from species other than $^1H_20$.

10. Concluding remarks

This review has summarized some recent developments in parallel imaging, a class of reconstruction methods that uses multiple receiver coils to accelerate MRI scans. Three historically important and clinically relevant techniques were described in detail—namely SENSE, GRAPPA, and SPIRiT. These techniques can be extended to non-Cartesian acquisitions and 3D MRI. Moreover, coil sensitivity information can be exploited to separate aliased slices in simultaneous multi-slice imaging. Phase information can also be incorporated to improve the conditioning of the parallel imaging reconstruction problem. Finally, MR spectroscopy imaging has intrinsically long scan times and is an excellent candidate for acceleration via parallel imaging.

It should be noted that parallel imaging is just one type of fast imaging reconstruction. Other methods that have not been covered in this review include compressed sensing (which exploits the fact that MR images are sparse under certain mathematical transforms) and k-t reconstructions (which exploit temporal correlations in dynamic datasets). These other methods are nearly always combined with parallel imaging to achieve even faster scan times. However, no other rapid imaging method has been as successful in a clinical setting as parallel imaging, and thus these methods based on coil sensitivity variations will continue to be essential for fast MRI.

Acknowledgments

Grant support was provided by Siemens Medical Solutions; United States National Institute of Health (NIH) T32EB007509, 2KL2TR000440; United States National Institute of Health and United States National Institute of Biomedical Imaging and Bioengineering (NIH/NIBIB) R00EB011527; United States National Heart, Lung, and Blood Institute (NHLBI) R01HL094557; United States National Institute of Diabetes and Digestive and Kidney Diseases (NIDDK) R01DK098503; National Science Foundation (NSF) CAREER CBET 1553441. Siemens, NIH, NIBIB, NHLBI, NIDDK, and NSF had no role in the preparation of this manuscript.

References

[1] P. Paolantonio, R. Ferrari, F. Vecchietti, S. Cucchiara, A. Laghi, Current status of MR imaging in the evaluation of IBD in a pediatric population of patients, Eur. J. Radiol. 69 (2009) 418–424.
[2] T.L. Lindholm, L. Botes, E.-L. Engman, A. Frank, T. Jonsson, L. Svensson, P. Julin, Parallel imaging: is GRAPPA a useful acquisition tool for MR imaging intended for volumetric brain analysis?, BMC Med Imag. 9 (2009) 15.
[3] S. Bhavsar, M. Zvyagintsev, K. Mathiak, BOLD sensitivity and SNR characteristics of parallel imaging-accelerated single-shot multi-echo EPI for fMRI, Neuroimage 84 (2014) 65–75.
[4] H. Li, K. Fox-Neff, B. Vaughan, D. French, J.P. Szaflarski, Y. Li, Parallel EPI artifact correction (PEAC) for N/2 ghost suppression in neuroimaging applications, Magn. Reson. Imag. 31 (2013) 1022–1028.
[5] A.E. Campbell-Washburn, A.Z. Faranesh, R.J. Lederman, M.S. Hansen, Magnetic resonance sequences and rapid acquisition for MR-guided interventions, Magn. Reson. Imag. Clin. N. Am. 23 (2015) 669–679.
[6] T. Zhang, J.Y. Cheng, A.G. Potnick, R.A. Barth, M.T. Alley, M. Uecker, M. Lustig, J. M. Pauly, S.S. Vasanawala, Fast pediatric 3D free-breathing abdominal dynamic contrast enhanced MRI with high spatiotemporal resolution, J. Magn. Reson. Imag. 41 (2015) 460–473.
[7] J.A. de Zwart, P. van Gelderen, X. Golay, V.N. Ikonomidou, J.H. Duyn, Accelerated parallel imaging for functional imaging of the human brain, NMR Biomed. 19 (2006) 342–351.
[8] C.B. Paschal, H.D. Morris, K-Space in the clinic, J. Magn. Reson. Imaging. 19 (2004) 145–159.
[9] M.S. Cohen, R.M. Weisskoff, R.R. Rzedzian, H.L. Kantor, Sensory stimulation by time-varying magnetic fields, Magn. Reson. Med. 14 (1990) 409–414.
[10] C.L.G. Ham, J.M.L. Engels, G.T. Van de Wiel, A. Machielsen, Peripheral nerve stimulation during MRI: effects of high gradient amplitudes and switching rates, J. Magn. Reson. Imag. 7 (1997) 933–937.
[11] A. Hoffmann, S.C. Faber, K.J. Werhahn, L. Jäger, M. Reiser, Electromyography in MRI - First recordings of peripheral nerve activation caused by fast magnetic field gradients, Magn. Reson. Med. 43 (2000) 534–539.
[12] D.I. Hoult, C.-N. Chen, V.J. Sank, The field dependence of NMR imaging 11. Arguments concerning an optimal field strength, Magn. Reson. Med. 3 (1986) 730–746.
[13] P.B. Roemer, W.A. Edelstein, C.E. Hayes, S.P. Souza, O.M. Mueller, The NMR phased array, Magn. Reson. Med. 16 (1990) 192–225.

[14] D. Walsh, A. Gmitro, M. Marcellin, Adaptive reconstruction of phased array MR imagery, Magn. Reson. Med. 43 (2000) 682–690.
[15] G.C. Wiggins, C. Triantafyllou, A. Potthast, A. Reykowski, M. Nittka, L.L. Wald, 32-Channel 3 T receive-only phased-array head coil with soccer-ball element geometry, Magn. Reson. Med. 56 (2006) 216–223.
[16] J. Cohen-Adad, A. Mareyam, B. Keil, J.R. Polimeni, L.L. Wald, 32-Channel RF coil optimized for brain and cervical spinal cord at 3 T, Magn. Reson. Med. 66 (2011) 1198–1208.
[17] B. Keil, J.N. Blau, S. Biber, P. Hoecht, V. Tountcheva, K. Setsompop, C. Triantafyllou, L.L. Wald, A 64-channel 3 T array coil for accelerated brain MRI, Magn. Reson. Med. 70 (2013) 248–258.
[18] G.C. Wiggins, J.R. Polimeni, A. Potthast, M. Schmitt, V. Alagappan, L.L. Wald, 96-Channel receive-only head coil for 3 T: design optimization and evaluation, Magn. Reson. Med. 62 (2009) 754–762.
[19] M. Schmitt, A. Potthast, D.E. Sosnovik, J.R. Polimeni, G.C. Wiggins, C. Triantafyllou, L.L. Wald, A 128-channel receive-only cardiac coil for highly accelerated cardiac MRI at 3 T, Magn. Reson. Med. 59 (2008) 1431–1439.
[20] K.P. Pruessmann, M. Weiger, M.B. Scheidegger, P. Boesiger, SENSE: sensitivity encoding for fast MRI, Magn. Reson. Med. 42 (1999) 952–962.
[21] P. Kellman, F.H. Epstein, E.R. McVeigh, Adaptive sensitivity encoding incorporating temporal filtering (TSENSE), Magn. Reson. Med. 45 (2001) 846–852.
[22] J. Wang, T. Kluge, M. Nittka, V. Jellus, B. Kuehn, B. Kiefer, Parallel acquisition techniques with modified SENSE reconstruction (mSENSE), in: Proceedings of the 1st Wü Rzbg. Work. Parallel Imaging, 2001, p. 92.
[23] J.B. Bell, A.N. Tikhonov, V.Y. Arsenin, Solutions of Ill-posed problems, Math. Comput. 32 (1978) 1320.
[24] K.T. Block, M. Uecker, J. Frahm, Undersampled radial MRI with multiple coils. Iterative image reconstruction using a total variation constraint, Magn. Reson. Med. 57 (2007) 1086–1098.
[25] L.I. Rudin, S. Osher, E. Fatemi, Nonlinear total variation based noise removal algorithms, Phys. D Nonlin. Phenom. 60 (1992) 259–268.
[26] Y. Guo, R.M. Lebel, Y. Zhu, S.G. Lingala, M.S. Shiroishi, M. Law, K. Nayak, High-resolution whole-brain DCE-MRI using constrained reconstruction: prospective clinical evaluation in brain tumor patients, Med. Phys. 43 (2016) 2013–2023.
[27] M.S. Hansen, T.S. Sørensen, A.E. Arai, P. Kellman, Retrospective reconstruction of high temporal resolution cine images from real-time MRI using iterative motion correction, Magn. Reson. Med. 68 (2012) 741–750.
[28] L. Feng, M.B. Srichai, R.P. Lim, A. Harrison, W. King, G. Adluru, E.V.R. Dibella, D. K. Sodickson, R. Otazo, D. Kim, Highly accelerated real-time cardiac cine MRI using k-t SPARSE-SENSE, Magn. Reson. Med. 74 (2012) 64–74.
[29] K.P. Pruessmann, M. Weiger, P. Boesiger, Sensitivity encoded cardiac MRI, J. Cardiovasc. Magn. Reson. 3 (2001) 1–9.
[30] M. Buehrer, M.E. Huber, F. Wiesinger, P. Boesiger, S. Kozerke, Coil setup optimization for 2D-SENSE whole-heart coronary imaging, Magn. Reson. Med. 55 (2006) 460–464.
[31] D.K. Sodickson, C.J. Hardy, Y. Zhu, R.O. Giaquinto, P. Gross, G. Kenwood, T. Niendorf, H. Lejay, C.A. McKenzie, M.A. Ohliger, A.K. Grant, N.M. Rofsky, Rapid volumetric MRI using parallel imaging with order-of-magnitude accelerations and a 32-element RF coil array: feasibility and implications, Acad. Radiol. 12 (2005) 626–635.
[32] W.A. Willinek, J. Gieseke, M. von Falkenhausen, M. Born, D. Hadizadeh, C. Manka, H.J. Textor, H.H. Schild, C.K. Kuhl, Sensitivity Encoding (SENSE) for High Spatial Resolution Time-of-Flight MR Angiography of the Intracranial Arteries at 3.0 T, RöFo - Fortschritte Auf Dem Gebiet Der Röntgenstrahlen Und Der Bildgeb. Verfahren 176 (2004) 21–26.
[33] R. Muthupillai, E. Douglas, S. Huber, B. Lambert, M. Pereyra, G.J. Wilson, S.D. Flamm, Direct comparison of sensitivity encoding (SENSE) accelerated and conventional 3D contrast enhanced magnetic resonance angiography (CE-MRA) of renal arteries: effect of increasing spatial resolution, J. Magn. Reson. Imag. 31 (2010) 149–159.
[34] M. Weiger, K.P. Pruessmann, A. Kassner, G. Roditi, T. Lawton, A. Reid, P. Boesiger, Contrast-enhanced 3D MRA using SENSE, J. Magn. Reson. Imag. 12 (2000) 671–677.
[35] G.J. Wilson, W.B. Eubank, G.B.C. Vasbinder, A.G.H. Kessels, R.M. Hoogeveen, R. Muthupillai, J.H. Maki, Utilising SENSE to reduce scan duration in high-resolution contrast-enhanced renal MR angiography, J. Magn. Reson. Imag. 24 (2006) 873–879.
[36] M. De Vries, R.J. Nijenhuis, R.M. Hoogeveen, M.W. De Haan, J.M.A. Van Engelshoven, T. Leiner, Contrast-enhanced peripheral MR angiography using SENSE in multiple stations: feasibility study, J. Magn. Reson. Imag. 21 (2005) 37–45.
[37] M.A. Griswold, P.M. Jakob, R.M. Heidemann, M. Nittka, V. Jellus, J. Wang, B. Kiefer, A. Haase, Generalized Autocalibrating Partially Parallel Acquisitions (GRAPPA), Magn. Reson. Med. 47 (2002) 1202–1210.
[38] S. Bauer, S. Bauer, M. Markl, M. Honal, B.A. Jung, The effect of reconstruction and acquisition parameters for GRAPPA-based parallel imaging on the image quality, Magn. Reson. Med. 66 (2011) 402–409.
[39] K. Uğurbil, J. Xu, E.J. Auerbach, S. Moeller, A.T. Vu, J.M. Duarte-Carvajalino, C. Lenglet, X. Wu, S. Schmitter, P.F. Van de Moortele, J. Strupp, G. Sapiro, F. De Martino, D. Wang, N. Harel, M. Garwood, L. Chen, D.A. Feinberg, S.M. Smith, K. L. Miller, S.N. Sotiropoulos, S. Jbabdi, J.L.R. Andersson, T.E.J. Behrens, M.F. Glasser, D.C. Van Essen, E. Yacoub, Pushing spatial and temporal resolution for functional and diffusion MRI in the human connectome project, Neuroimage 80 (2013) 80–104.
[40] F.A. Breuer, P. Kellman, M.A. Griswold, P.M. Jakob, Dynamic autocalibrated parallel imaging using temporal GRAPPA (TGRAPPA), Magn. Reson. Med. 53 (2005) 981–985.
[41] F.A. Breuer, S.A.R. Kannengiesser, M. Blaimer, N. Seiberlich, P.M. Jakob, M.A. Griswold, General formulation for quantitative G-factor calculation in GRAPPA reconstructions, Magn. Reson. Med. 62 (2009) 739–746.
[42] M.A. Griswold, S. Kannengiesser, R.M. Heidemann, J. Wang, P.M. Jakob, Field-of-view limitations in parallel imaging, Magn. Reson. Med. 52 (2004) 1118–1126.
[43] F. Schwab, F. Schwarz, O. Dietrich, T. Lanz, F. Resmer, T. Wichmann, B.J. Wintersperger, F. Bamberg, K. Nikolaou, M. Reiser, D. Theisen, Free breathing real-time cardiac cine imaging with improved spatial resolution at 3 T, Invest. Radiol. 48 (2013) 158–166.
[44] P. Hunold, S. Maderwald, M.E. Ladd, V. Jellus, J. Barkhausen, Parallel acquisition techniques in cardiac cine magnetic resonance imaging using TrueFISP sequences: comparison of image quality and artifacts, J. Magn. Reson. Imag. 20 (2004) 506–511.
[45] D. Theisen, T.A. Sandner, F. Bamberg, K.U. Bauner, F. Schwab, F. Schwarz, E. Arnoldi, M.F. Reiser, B.J. Wintersperger, High-resolution cine MRI with TGRAPPA for fast assessment of left ventricular function at 3 T, Eur. J. Radiol. 82 (2013).
[46] T. Breyer, M. Echternach, S. Arndt, B. Richter, O. Speck, M. Schumacher, M. Markl, Dynamic magnetic resonance imaging of swallowing and laryngeal motion using parallel imaging at 3 T, Magn. Reson. Imag. 27 (2009) 48–54.
[47] H. Saybasili, P. Kellman, M.A. Griswold, J.A. Derbyshire, M.A. Guttman, HTGRAPPA: real-time B1-weighted image domain TGRAPPA reconstruction, Magn. Reson. Med. 61 (2009) 1425–1433.
[48] M. Bock, S. Müller, S. Zuehlsdorff, P. Speier, C. Fink, P. Hallscheidt, R. Umathum, W. Semmler, Active catheter tracking using parallel MRI and real-time image reconstruction, Magn. Reson. Med. 55 (2006) 1454–1459.
[49] I. Nölte, L. Gerigk, M.A. Brockmann, A. Kemmling, C. Groden, MRI of degenerative lumbar spine disease: comparison of non-accelerated and parallel imaging, Neuroradiology 50 (2008) 403–409.
[50] I.M. Noebauer-Huhmann, C. Glaser, O. Dietrich, C.P. Wallner, W. Klinger, H. Imhof, S.O. Schoenberg, MR imaging of the cervical spine: assessment of image quality with parallel imaging compared to non-accelerated MR measurements, Eur. Radiol. 17 (2007) 1147–1155.
[51] J. Fruehwald-Pallamar, P. Szomolanyi, N. Fakhrai, A. Lunzer, M. Weber, M.M. Thurnher, M. Pallamar, S. Trattnig, D. Prayer, I.M. Noebauer-Huhmann, Parallel imaging of the cervical spine at 3 T: optimized trade-off between speed and image quality, Am. J. Neuroradiol. 33 (2012) 1867–1874.
[52] N. Zhang, L. Zou, Y. Huang, D. Liu, Y. Tang, Z. Fan, H. Chen, X. Liu, Non-contrast enhanced MR angiography (NCE-MRA) of the calf: a direct comparison between flow-sensitive dephasing (FSD) prepared steady-state free precession (SSFP) and quiescent-interval single-shot (QISS) in patients with diabetes, PLoS ONE 10 (2015).
[53] L. Armstrong, J.C.L. Rodrigues, C.B. Lawton, J. Tyrell-Price, M.C.K. Hamilton, N. E. Manghat, Application of TWIST MR angiography to aid successful central venous access in challenging patients: initial single-centre experience, Clin. Radiol. 71 (2016) 1104–1112.
[54] Y.V. Chang, J.D. Quirk, D.A. Yablonskiy, In vivo lung morphometry with accelerated hyperpolarized 3He diffusion MRI: a preliminary study, Magn. Reson. Med. 73 (2015) 1609–1614.
[55] J. Rivoire, F. Meise, M. Terekhov, D. Santoro, Z. Salhi, W. Schreiber, Comparison of different parallel imaging reconstruction methods for hyperpolarized 3He MRI, in: Proceedings of the 17th Science Meeting of the International Society of Magnetic Resonance in Medicine, Honolulu, 2009, p. 2168.
[56] S. Skare, R.D. Newbould, D.B. Clayton, G.W. Albers, S. Nagle, R. Bammer, Clinical multishot DW-EPI through parallel imaging with considerations of susceptibility, motion, and noise, Magn. Reson. Med. 57 (2007) 881–890.
[57] D.A. Porter, R.M. Heidemann, High resolution diffusion-weighted imaging using readout-segmented echo-planar imaging, parallel imaging and a two-dimensional navigator-based reacquisition, Magn. Reson. Med. 62 (2009) 468–475.
[58] W.S. Hoge, J.R. Polimeni, Dual-polarity GRAPPA for simultaneous reconstruction and ghost correction of echo planar imaging data, Magn. Reson. Med. 76 (2016) 32–44.
[59] E.Y. Pierre, D. Grodzki, G. Aandal, B. Heismann, C. Badve, V. Gulani, J.L. Sunshine, M. Schluchter, K. Liu, M.A. Griswold, Parallel imaging-based reduction of acoustic noise for clinical magnetic resonance imaging, Invest. Radiol. 49 (2014) 620–626.
[60] M. Lustig, J.M. Pauly, SPIRiT: Iterative self-consistent parallel imaging reconstruction from arbitrary k-space, Magn. Reson. Med. 64 (2010) 457–471.
[61] M. Murphy, M. Alley, J. Demmel, K. Keutzer, S. Vasanawala, M. Lustig, Fast l_1-SPIRiT compressed sensing parallel imaging MRI: scalable parallel implementation and clinically feasible runtime, IEEE Trans. Med. Imag. 31 (2012) 1250–1262.
[62] M. Uecker, P. Lai, M.J. Murphy, P. Virtue, M. Elad, J.M. Pauly, S.S. Vasanawala, M. Lustig, ESPIRiT - an eigenvalue approach to autocalibrating parallel MRI: where SENSE meets GRAPPA, Magn. Reson. Med. 71 (2014) 990–1001.
[63] S.S. Vasanawala, M.J. Murphy, M.T. Alley, P. Lai, K. Keutzer, J.M. Pauly, M. Lustig, Practical parallel imaging compressed sensing MRI: Summary of two years of experience in accelerating body MRI of pediatric patients, in: Proceedings of the International Symposium on Biomedical Imaging, 2011, pp. 1039–1043.

[64] T. Zhang, S. Chowdhury, M. Lustig, R.A. Barth, M.T. Alley, T. Grafendorfer, P.D. Calderon, F.J.L. Robb, J.M. Pauly, S.S. Vasanawala, Clinical performance of contrast enhanced abdominal pediatric MRI with fast combined parallel imaging compressed sensing reconstruction, J. Magn. Reson. Imag. 40 (2014) 13–25.

[65] H. Xue, P. Kellman, G. LaRocca, A.E. Arai, M.S. Hansen, High spatial and temporal resolution retrospective cine cardiovascular magnetic resonance from shortened free breathing real-time acquisitions, J. Cardiovasc. Magn. Reson. 15 (2013) 102.

[66] B.M.A. Delattre, R.M. Heidemann, L.A. Crowe, J.-P. Vallée, J.-N. Hyacinthe, Spiral demystified, Magn. Reson. Imag. 28 (2010) 862–881.

[67] J. Fessler, B. Sutton, Nonuniform fast Fourier transforms using min-max interpolation, IEEE Trans. Signal Process. 51 (2003) 560–574.

[68] J. Jackson, C. Meyer, D. Nishimura, A. Macovski, Selection of a convolution function for Fourier inversion using gridding, IEEE Trans. Med. Imag. 10 (1991) 473–478.

[69] K.P. Pruessmann, M. Weiger, P. Bornert, P. Boesiger, Advances in sensitivity encoding with arbitrary k-space trajectories, Magn. Reson. Med. 46 (2001) 638–651.

[70] N. Seiberlich, P. Ehses, J. Duerk, R. Gilkeson, M. Griswold, Improved radial GRAPPA calibration for real-time free-breathing cardiac imaging, Magn. Reson. Med. 65 (2011) 492–505.

[71] N. Seiberlich, G. Lee, P. Ehses, J.L. Duerk, R. Gilkeson, M. Griswold, Improved temporal resolution in cardiac imaging using through-time spiral GRAPPA, Magn. Reson. Med. 66 (2011) 1682–1688.

[72] K.L. Wright, G.R. Lee, P. Ehses, M.A. Griswold, V. Gulani, N. Seiberlich, Three-dimensional through-time radial GRAPPA for renal MR angiography, J. Magn. Reson. Imag. 40 (2014) 864–874.

[73] M. Griswold, R. Heidemann, P. Jakob, Direct parallel imaging reconstruction of radially sampled data using GRAPPA with relative shifts, in: Proceedings ff the 11th Annual Meeting of ISMRM, Toronto, Canada, 2003, p. 2349.

[74] R.M. Heidemann, M.A. Griswold, N. Seiberlich, G. Krüger, S.A.R. Kannengiesser, B. Kiefer, G. Wiggins, L.L. Wald, P.M. Jakob, Direct parallel image reconstructions for spiral trajectories using GRAPPA, Magn. Reson. Med. 56 (2006) 317–326.

[75] D.C. Noll, Multishot rosette trajectories for spectrally selective MR imaging, IEEE Trans. Med. Imag. 16 (1997) 372–377.

[76] J.G. Pipe, Motion correction with PROPELLER MRI: application to head motion and free-breathing cardiac imaging, Magn. Reson. Med. 42 (1999) 963–969.

[77] S. Skare, R.D. Newbould, A. Nordell, S.J. Holdsworth, R. Bammer, An auto-calibrated, angularly continuous, two-dimensional GRAPPA kernel for propeller trajectories, Magn. Reson. Med. 60 (2008) 1457–1465.

[78] H. Saybasili, D.A. Herzka, N. Seiberlich, M.A. Griswold, Real-time imaging with radial GRAPPA: implementation on a heterogeneous architecture for low-latency reconstructions, Magn. Reson. Imag. 32 (2014) 747–758.

[79] L. Feng, R. Grimm, K.T. obias Block, H. Chandarana, S. Kim, J. Xu, L. Axel, D.K. Sodickson, R. Otazo, Golden-angle radial sparse parallel MRI: combination of compressed sensing, parallel imaging, and golden-angle radial sampling for fast and flexible dynamic volumetric MRI, Magn. Reson. Med. 72 (2014) 707–717.

[80] L. Feng, L. Axel, H. Chandarana, K.T. Block, D.K. Sodickson, R. Otazo, XD-GRASP: golden-angle radial MRI with reconstruction of extra motion-state dimensions using compressed sensing, Magn. Reson. Med. 75 (2016) 775–788.

[81] R. Nezafat, P. Kellman, J.A. Derbyshire, E.R. McVeigh, Real-time blood flow imaging using autocalibrated spiral sensitivity encoding, Magn. Reson. Med. 54 (2005) 1557–1561.

[82] G. Aandal, V. Nadig, V. Yeh, P. Rajiah, T. Jenkins, A. Sattar, M. Griswold, V. Gulani, R.C. Gilkeson, N. Seiberlich, Evaluation of left ventricular ejection fraction using through-time radial GRAPPA, J. Cardiovasc. Magn. Reson. 16 (2014) 79.

[83] J.I. Hamilton, K. Barkauskas, N. Seiberlich, Accelerated 2D multi-slice first-pass contrast-enhanced myocardial perfusion using through-time radial GRAPPA, J. Cardiovasc. Magn. Reson. 16 (2014) P378.

[84] Y. Chen, G.R. Lee, K. Wright, M.A. Griswold, N. Seiberlich, V. Gulani, Multiphasic contrast enhanced free breathing 3D imaging and liver perfusion mapping using through-time 3D spiral GRAPPA acceleration, in: Proceedings of the 99th Annual Meeting of the Radiological Society of North America, 2013, p. SST06-03.

[85] Y. Chen, G.R. Lee, G. Aandal, C. Badve, K.L. WrighT, M.A. Griswold, N. Seiberlich, V. Gulani, Rapid volumetric T1 mapping of the abdomen using three-dimensional through-time spiral GRAPPA, Magn. Reson. Med. 75 (2016) 1457–1465.

[86] T. Shin, M. Lustig, D.G. Nishimura, B.S. Hu, Rapid single-breath-hold 3D late gadolinium enhancement cardiac MRI using a stack-of-spirals acquisition, J. Magn. Reson. Imag. 40 (2014) 1496–1502.

[87] C. Santelli, T. Schaeffter, S. Kozerke, Radial k-t SPIRiT: autocalibrated parallel imaging for generalized phase-contrast MRI, Magn. Reson. Med. 72 (2014) 1233–1245.

[88] D.M. Lyra-Leite, J.L.A. Carvalho, Parallel imaging acceleration of spiral Fourier velocity encoded MRI using SPIRiT, in: Proceedings of the Annual International Conference of IEEE Engineering in Medicine and Biology Society, EMBS, 2012, pp. 416–419.

[89] Y.-C. Kim, R.M. Lebel, Z. Wu, S.L.D. Ward, M.C.K. Khoo, K.S. Nayak, Real-time 3D magnetic resonance imaging of the pharyngeal airway in sleep apnea, Magn. Reson. Med. 71 (2014) 1501–1510.

[90] T.S. Sorensen, D. Atkinson, T. Schaeffter, M.S. Hansen, Real-time reconstruction of sensitivity encoded radial magnetic resonance imaging using a graphics processing unit, IEEE Trans. Med. Imag. 28 (2009) 1974–1985.

[91] O. Sayin, H. Saybasili, M.M. Zviman, M. Griswold, H. Halperin, N. Seiberlich, D. A. Herzka, Real-time free-breathing cardiac imaging with self-calibrated through-time radial GRAPPA, Magn. Reson. Med. 77 (2017) 250–264.

[92] D.J. Larkman, J.V. Hajnal, A.H. Herlihy, G.A. Coutts, I.R. Young, G. Ehnholm, Use of multicoil arrays for separation of signal from multiple slices simultaneously excited, J. Magn. Reson. Imag. 13 (2001) 313–317.

[93] M. Barth, F. Breuer, P.J. Koopmans, D.G. Norris, B.A. Poser, Simultaneous multislice (SMS) imaging techniques, Magn. Reson. Med. 75 (2016) 63–81.

[94] B.A. Hargreaves, C.H. Cunningham, D.G. Nishimura, S.M. Conolly, Variable-rate selective excitation for rapid MRI sequences, Magn. Reson. Med. 52 (2004) 590–597.

[95] D.G. Norris, P.J. Koopmans, R. Boyacioğlu, M. Barth, Power independent of number of slices (PINS) radiofrequency pulses for low-power simultaneous multislice excitation, Magn. Reson. Med. 66 (2011) 1234–1240.

[96] C. Eichner, L.L. Wald, K. Setsompop, A low power radiofrequency pulse for simultaneous multislice excitation and refocusing, Magn. Reson. Med. 72 (2014) 949–958.

[97] K. Setsompop, J. Cohen-Adad, B.A. Gagoski, T. Raij, A. Yendiki, B. Keil, V.J. Wedeen, L.L. Wald, Improving diffusion MRI using simultaneous multi-slice echo planar imaging, Neuroimage 63 (2012) 569–580.

[98] A.Z. Lau, E.M. Tunnicliffe, R. Frost, P.J. Koopmans, D.J. Tyler, M.D. Robson, Accelerated human cardiac diffusion tensor imaging using simultaneous multislice imaging, Magn. Reson. Med. 73 (2015) 995–1004.

[99] D.A. Feinberg, K. Setsompop, Ultra-fast MRI of the human brain with simultaneous multi-slice imaging, J. Magn. Reson. 229 (2013) 90–100.

[100] D.A. Feinberg, S. Moeller, S.M. Smith, E. Auerbach, S. Ramanna, M.F. Glasser, K. L. Miller, K. Ugurbil, E. Yacoub, Multiplexed echo planar imaging for sub-second whole brain FMRI and fast diffusion imaging, PLoS ONE 5 (2010) e15710.

[101] B. Zahneisen, B.A. Poser, T. Ernst, A.V. Stenger, Simultaneous multi-slice fMRI using spiral trajectories, Neuroimage 92 (2014) 8–18.

[102] F.A. Breuer, M. Blaimer, R.M. Heidemann, M.F. Mueller, M.A. Griswold, P.M. Jakob, Controlled aliasing in parallel imaging results in higher acceleration (CAIPIRINHA) for multi-slice imaging, Magn. Reson. Med. 53 (2005) 684–691.

[103] G.H. Glover, Phase-offset multiplanar (POMP) volume imaging: A new technique, J. Magn. Reson. Imag. 1 (1991) 457–461.

[104] D. Stäb, C.O. Ritter, F.A. Breuer, A.M. Weng, D. Hahn, H. Köstler, CAIPIRINHA accelerated SSFP imaging, Magn. Reson. Med. 65 (2011) 157–164.

[105] K. Setsompop, B.A. Gagoski, J.R. Polimeni, T. Witzel, V.J. Wedeen, L.L. Wald, Blipped-controlled aliasing in parallel imaging for simultaneous multislice echo planar imaging with reduced g-factor penalty, Magn. Reson. Med. 67 (2012) 1210–1224.

[106] R.G. Nunes, J.V Hajnal, X. Golay, D.J. Larkman, Simultaneous slice excitation and reconstruction for single shot EPI, in: Proceedings of ISMRM, vol. 14, 2006, p. 293.

[107] S.R. Yutzy, N. Seiberlich, J.L. Duerk, M.A. Griswold, Improvements in multislice parallel imaging using radial CAIPIRINHA, Magn. Reson. Med. 65 (2011) 1630–1637.

[108] M. Blaimer, F.A. Breuer, N. Seiberlich, M.F. Mueller, R.M. Heidemann, V. Jellus, G. Wiggins, L.L. Wald, M.A. Griswold, P.M. Jakob, Accelerated volumetric MRI with a SENSE/GRAPPA combination, J. Magn. Reson. Imag. 24 (2006) 444–450.

[109] S. Moeller, J. Xu, E. Auerbach, E. Yacoub, K. Ugurbil, Signal leakage (l-factor) as a measure of parallel imaging performance among simultaneously multislice (SMS) excited and acquired signals, in: Proceedings of the 20th Annual Meeting of ISMRM, Melbourne, Australia, 2012, p. 519.

[110] S.F. Cauley, J.R. Polimeni, H. Bhat, L.L. Wald, K. Setsompop, Interslice leakage artifact reduction technique for simultaneous multislice acquisitions, Magn. Reson. Med. 72 (2014) 93–102.

[111] L. Chen, A.T. Vu, J. Xu, S. Moeller, K. Ugurbil, E. Yacoub, D.A. Feinberg, Evaluation of highly accelerated simultaneous multi-slice EPI for fMRI, Neuroimage 104 (2015) 452–459.

[112] L. Filli, S. Ghafoor, D. Kenkel, W. Liu, E. Weiland, G. Andreisek, T. Frauenfelder, V.M. Runge, A. Boss, Simultaneous multi-slice readout-segmented echo planar imaging for accelerated diffusion-weighted imaging of the breast, Eur. J. Radiol. 85 (2016) 274–278.

[113] D. Stäb, T. Wech, F.A. Breuer, A.M. Weng, C.O. Ritter, D. Hahn, H. Köstler, High resolution myocardial first-pass perfusion imaging with extended anatomic coverage, J. Magn. Reson. Imag. 39 (2014) 1575–1587.

[114] H. Wang, G. Adluru, L. Chen, E.G. Kholmovski, N.K. Bangerter, E.V.R. DiBella, Radial simultaneous multi-slice CAIPI for ungated myocardial perfusion, Magn. Reson. Imag. 34 (2016) 1329–1336.

[115] Z. Wu, W. Chen, M.C.K. Khoo, S.L. Davidson Ward, K.S. Nayak, Evaluation of upper airway collapsibility using real-time MRI, J. Magn. Reson. Imag. 44 (2016) 158–167.

[116] Z. Celicanin, O. Bieri, F. Preiswerk, P. Cattin, K. Scheffler, F. Santini, Simultaneous acquisition of image and navigator slices using CAIPIRINHA for 4D MRI, Magn. Reson. Med. 73 (2015) 669–676.

[117] Y. Wang, X. Shao, T. Martin, S. Moeller, E. Yacoub, D.J.J. Wang, Phase-cycled simultaneous multislice balanced SSFP imaging with CAIPIRINHA for efficient banding reduction, Magn. Reson. Med. 76 (2016) 1764–1774.

[118] M. Weiger, K.P. Pruessmann, P. Boesiger, 2D SENSE for faster 3D MRI, Magn. Reson. Mater. Phys. Biol. Med. 14 (2002) 10–19.
[119] M. Blaimer, F.A. Breuer, M. Mueller, N. Seiberlich, D. Ebel, R.M. Heidemann, M. A. Griswold, P.M. Jakob, 2D-GRAPPA-operator for faster 3D parallel MRI, Magn. Reson. Med. 56 (2006) 1359–1364.
[120] F.A. Breuer, M. Blaimer, M.F. Mueller, N. Seiberlich, R.M. Heidemann, M.A. Griswold, P.M. Jakob, Controlled aliasing in volumetric parallel imaging (2D CAIPIRINHA), Magn. Reson. Med. 55 (2006) 549–556.
[121] P.T. Weavers, E.A. Borisch, S.J. Riederer, Selection and evaluation of optimal two-dimensional CAIPIRINHA Kernels applied to time-resolved three-dimensional CE-MRA, Magn. Reson. Med. 73 (2015) 2234–2242.
[122] K.L. Wright, M.W. Harrell, J.A. Jesberger, L. Landeras, D.A. Nakamoto, S. Thomas, D. Nickel, R. Kroeker, M.A. Griswold, V. Gulani, Clinical evaluation of CAIPIRINHA: comparison against a GRAPPA standard, J. Magn. Reson. Imag. 39 (2014) 189–194.
[123] M.H. Yu, J.M. Lee, J.H. Yoon, B. Kiefer, J.K. Han, B.I. Choi, Clinical application of controlled aliasing in parallel imaging results in a higher acceleration (CAIPIRINHA)-volumetric interpolated breathhold (VIBE) sequence for gadoxetic acid-enhanced liver MR imaging, J. Magn. Reson. Imag. 38 (2013) 1020–1026.
[124] B. Kim, C.K. Lee, N. Seo, S.S. Lee, J.K. Kim, Y. Choi, D.C. Woo, I.S. Kim, D. Nickel, K.W. Kim, Comparison of CAIPIRINHA-VIBE, Radial-VIBE, and conventional VIBE sequences for dynamic contrast-enhanced (DCE) MRI: a validation study using a DCE-MRI phantom, Magn. Reson. Imag. 34 (2016) 638–644.
[125] J. Huh, Y. Choi, D.C. Woo, N. Seo, B. Kim, C.K. Lee, I.S. Kim, D. Nickel, K.W. Kim, Feasibility of test-bolus DCE-MRI using CAIPIRINHA-VIBE for the evaluation of pancreatic malignancies, Eur. Radiol. 26 (2016) 3949–3956.
[126] H.J. Michaely, J.N. Morelli, J. Budjan, P. Riffel, D. Nickel, R. Kroeker, S.O. Schoenberg, U.I. Attenberger, CAIPIRINHA-Dixon-TWIST (CDT)–Volume-Interpolated Breath-Hold Examination (VIBE), Invest. Radiol. 48 (2013) 590–597.
[127] J. Fritz, B. Fritz, G.G. Thawait, H. Meyer, W.D. Gilson, E. Raithel, Three-dimensional CAIPIRINHA SPACE TSE for 5-minute high-resolution MRI of the Knee, Invest. Radiol. (2016) 1.
[128] B. Bilgic, B.A. Gagoski, S.F. Cauley, A.P. Fan, J.R. Polimeni, P.E. Grant, L.L. Wald, K. Setsompop, Wave-CAIPI for highly accelerated 3D imaging, Magn. Reson. Med. 73 (2015) 2152–2162.
[129] J.D. Willig-Onwuachi, E.N. Yeh, A.K. Grant, M.A. Ohliger, C.A. McKenzie, D.K. Sodickson, Phase-constrained parallel MR image reconstruction, J. Magn. Reson. 176 (2005) 187–198.
[130] M. Bydder, M.D. Robson, Partial fourier partially parallel imaging, Magn. Reson. Med. 53 (2005) 1393–1401.
[131] M. Blaimer, P.M. Jakob, F.A. Breuer, Regularization method for phase-constrained parallel MRI, Magn. Reson. Med. 72 (2014) 166–171.
[132] C. Lew, A.R. Pineda, D. Clayton, D. Spielman, F. Chan, R. Bammer, SENSE phase-constrained magnitude reconstruction with iterative phase refinement, Magn. Reson. Med. 58 (2007) 910–921.
[133] M. Blaimer, M. Gutberlet, P. Kellman, F.A. Breuer, H. Köstler, M.A. Griswold, Virtual coil concept for improved parallel MRI employing conjugate symmetric signals, Magn. Reson. Med. 61 (2009) 93–102.
[134] J.P. Haldar, Low-rank modeling of local k-space neighborhoods (LORAKS) for constrained MRI, IEEE Trans. Med. Imag. 33 (2014) 668–681.
[135] P.J. Shin, P.E.Z. Larson, M.A. Ohliger, M. Elad, J.M. Pauly, D.B. Vigneron, M. Lustig, Calibrationless parallel imaging reconstruction based on structured low-rank matrix completion, Magn. Reson. Med. 72 (2014) 959–970.
[136] J.P. Haldar, J. Zhuo, P-LORAKS: Low-rank modeling of local k-space neighborhoods with parallel imaging data, Magn. Reson. Med. 75 (2016) 1499–1514.
[137] T.H. Kim, K. Setsompop, J.P. Haldar, LORAKS makes better SENSE: Phase-constrained partial fourier SENSE reconstruction without phase calibration, Magn. Reson. Med. (2016) n/a–n/a.
[138] M. Blaimer, M. Heim, D. Neumann, P.M. Jakob, S. Kannengiesser, F.A. Breuer, Comparison of phase-constrained parallel MRI approaches: analogies and differences, Magn. Reson. Med. 75 (2016) 1086–1099.
[139] J. Schneider, M. Blaimer, P. Ullmann, Tailoring the image background phase by spatially selective excitation for improved parallel imaging reconstruction performance, in: Proceedings of the 20th Annual Meeting of ISMRM, Melbourne, Australia, 2012, p. 516.
[140] M. Zaitsev, G. Schultz, J. Hennig, R. Gruetter, D. Gallichan, Parallel imaging with phase scrambling, Magn. Reson. Med. 73 (2015) 1407–1419.
[141] M. Blaimer, M. Choli, P.M. Jakob, M.A. Griswold, F.A. Breuer, Multiband phase-constrained parallel MRI, Magn. Reson. Med. 69 (2013) 974–980.
[142] T.H. Kim, J.P. Haldar, SMS-LORAKS: calibrationless simultaneous multislice MRI using low-rank matrix modeling, in: 2015 IEEE 12th International Symposium on Biomedical Imaging, IEEE, 2015, pp. 323–326.
[143] S. Posse, R. Otazo, S.R. Dager, J. Alger, MR spectroscopic imaging: principles and recent advances, J. Magn. Reson. Imag. 37 (2013) 1301–1325.
[144] U. Dydak, M. Weiger, K.P. Pruessmann, D. Meier, P. Boesiger, Sensitivity-encoded spectroscopic imaging, Magn. Reson. Med. 46 (2001) 713–722.
[145] J. Ruff, N. Seiberlich, P. Jakob, M. Griswold, M. Blaimer, D. Ebel, F. Breuer, Parallel 2D and 3D spectroscopic imaging using GRAPPA, in: Proceedings of the 14th Science Meeting of the International Society of Magnetic Resonance in Medicine, 2006, p. 3653.
[146] B. Strasser, M. Považan, G. Hangel, L. Hingerl, M. Chmelik, S. Gruber, S. Trattnig, W. Bogner, (2 + 1)D-CAIPIRINHA accelerated MR spectroscopic imaging of the brain at 7 T, Magn. Reson. Med. (2016), http://dx.doi.org/10.1002/mrm.26386.
[147] U. Dydak, K.P. Pruessmann, M. Weiger, J. Tsao, D. Meier, P. Boesiger, Parallel spectroscopic imaging with spin-echo trains, Magn. Reson. Med. 50 (2003) 196–200.
[148] F.-H. Lin, S.-Y. Tsai, R. Otazo, A. Caprihan, L.L. Wald, J.W. Belliveau, S. Posse, Sensitivity-encoded (SENSE) proton echo-planar spectroscopic imaging (PEPSI) in the human brain, Magn. Reson. Med. 57 (2007) 249–257.
[149] X. Zhu, A. Ebel, J.X. Ji, N. Schuff, Spectral phase-corrected GRAPPA reconstruction of three-dimensional echo-planar spectroscopic imaging (3D-EPSI), Magn. Reson. Med. 57 (2007) 815–820.
[150] S.Y. Tsai, R. Otazo, S. Posse, Y.R. Lin, H.W. Chung, L.L. Wald, G.C. Wiggins, F.H. Lin, Accelerated proton echo planar spectroscopic imaging (PEPSI) using GRAPPA with a 32-channel phased-array coil, Magn. Reson. Med. 59 (2008) 989–998.
[151] S. Posse, R. Otazo, S.-Y. Tsai, A.E. Yoshimoto, F.-H. Lin, Single-shot magnetic resonance spectroscopic imaging with partial parallel imaging, Magn. Reson. Med. 61 (2009) 541–547.
[152] D. Mayer, D.H. Kim, D.M. Spielman, R. Bammer, Fast parallel spiral chemical shift imaging at 3T using iterative SENSE reconstruction, Magn. Reson. Med. 59 (2008) 891–897.
[153] M. Gu, C. Liu, D.M. Spielman, Parallel spectroscopic imaging reconstruction with arbitrary trajectories using k-space sparse matrices, Magn. Reson. Med. 61 (2009) 267–272.
[154] J. Frahm, K.-D. Merboldt, W. Hänicke, Localized proton spectroscopy using stimulated echoes, J. Magn. Reson. 72 (1987) 502–508.
[155] P.A. Bottomley, Spatial localization in NMR spectroscopy in vivo, Ann. N.Y. Acad. Sci. 508 (1987) 333–348.
[156] V.O. Boer, D.W.J. Klomp, J. Laterra, P.B. Barker, Parallel reconstruction in accelerated multivoxel MR spectroscopy, Magn. Reson. Med. 74 (2015) 599–606.
[157] H. Zhu, B.J. Soher, R. Ouwerkerk, M. Schar, P.B. Barker, Spin-echo magnetic resonance spectroscopic imaging at 7 T with frequency-modulated refocusing pulses, Magn. Reson. Med. 69 (2013) 1217–1225.
[158] G. Hangel, B. Strasser, M. Považan, S. Gruber, M. Chmelík, M. Gajdošík, S. Trattnig, W. Bogner, Lipid suppression via double inversion recovery with symmetric frequency sweep for robust 2D-GRAPPA-accelerated MRSI of the brain at 7 T, NMR Biomed. 28 (2015) 1413–1425.
[159] K. Golman, R. in 't Zandt, M. Thaning, Real-time metabolic imaging, Proc. Natl. Acad. Sci. USA 103 (2006) 11270–11275.
[160] J. Kurhanewicz, D.B. Vigneron, K. Brindle, E.Y. Chekmenev, A. Comment, C.H. Cunningham, R.J. Deberardinis, G.G. Green, M.O. Leach, S.S. Rajan, R.R. Rizi, B. D. Ross, W.S. Warren, C.R. Malloy, Analysis of cancer metabolism by imaging hyperpolarized nuclei: prospects for translation to clinical research, Neoplasia 13 (2011) 81–97.
[161] A. Arunachalam, D. Whitt, K. Fish, R. Giaquinto, J. Piel, R. Watkins, I. Hancu, Accelerated spectroscopic imaging of hyperpolarized C-13 pyruvate using SENSE parallel imaging, NMR Biomed. 22 (2009) 867–873.
[162] P.J. Shin, P.E.Z. Larson, M. Uecker, G.D. Reed, A.B. Kerr, J. Tropp, M.A. Ohliger, S. J. Nelson, J.M. Pauly, M. Lustig, D.B. Vigneron, Chemical shift separation with controlled aliasing for hyperpolarized 13C metabolic imaging, Magn. Reson. Med. 74 (2015) 978–989.
[163] M. Sabati, J. Zhan, V. Govind, K.L. Arheart, A.A. Maudsley, Impact of reduced k-space acquisition on pathologic detectability for volumetric MR spectroscopic imaging, J. Magn. Reson. Imag. 39 (2014) 224–234.

Glossary

ACS: autocalibration signal
BOLD: blood oxygenation level dependent
bSSFP: balanced steady-state free precession
CAIPIRINHA: Controlled Aliasing in Parallel Imaging Results in Higher Acceleration
CG: conjugate gradient
CSI: chemical shift imaging
DCE: dynamic contrast-enhanced
DFT: Discrete Fourier Transform
EPI: echo planar imaging
EPSI: echo planar spectroscopic imaging
ESPIRiT: SPIRiT using eigenvector maps
fMRI: functional Magnetic Resonance Imaging
FID: free induction decay
FLASH: Fast Low Angle SHot
FOV: field of view
g-factor: geometry factor
GRAPPA: GeneRalized Autocalibrating Partial Parallel Acquisition
GRASP: Golden-angle RAdial Sparse Parallel MRI
LGE: late gadolinium enhancement
LORAKS: low-rank modeling of local k-space neighborhoods
MB: multiband factor
MRA: magnetic resonance angiography
MRSI: magnetic resonance spectroscopic imaging
mSENSE: modified SENSitivity Encoding
NUFFT: Non-Uniform Fast Fourier Transform

PC-SENSE: Phase-Constrained SENSitivity Encoding
PINS: Power Independent of Number of Slices
POMP: Phase-offset multiplanar imaging
PRESS: Point-RESolved Spectroscopy
PSF: point spread function
R: acceleration factor
RF: radiofrequency
SAR: specific absorption rate
SENSE: SENSitivity Encoding
SMS: simultaneous multi-slice
SNR: signal-to-noise ratio
SPIRiT: iTerative Self-consistent Parallel Imaging Reconstruction
STEAM: STimulated Echo Acquisition Mode
SV-MRS: single-voxel magnetic resonance spectroscopy
TGRAPPA: Temporal GRAPPA
TR: repetition time
TSE: turbo spin echo
TSENSE: Time-adaptive SENSitivity Encoding
VCC-SENSE: Virtual Conjugate Coil SENSitivity Encoding
VERSE: Variable-rate selective excitation